

Microstructural evolution and mechanical properties of nano-ATZ ceramics by solid solution precipitation

Yongdong Yu

Harbin Institute of Technology

Xudong Liu

Harbin Institute of Technology

Yuchen Yuan

Harbin Institute of Technology

Wanjun Yu

Yantai University

Hang Yin

Harbin Institute of Technology

Zhao Yin

Harbin Institute of Technology

Y.T. Zheng (✉ zhengyt@hit.edu.cn)

Harbin Institute of Technology <https://orcid.org/0000-0001-8509-2132>

Xiaodong He

Harbin Institute of Technology

Research Article

Keywords: Microstructural evolution, Nano-ATZ, Solid solutions, Nanoprecipitation

Posted Date: June 11th, 2021

DOI: <https://doi.org/10.21203/rs.3.rs-607250/v1>

License: © ⓘ This work is licensed under a Creative Commons Attribution 4.0 International License.

[Read Full License](#)

Version of Record: A version of this preprint was published at Journal of Materials Research and Technology on December 1st, 2021. See the published version at <https://doi.org/10.1016/j.jmrt.2021.12.057>.

Microstructural evolution and mechanical properties of nano-ATZ ceramics by solid solution precipitation

Yongdong Yu¹, Xudong Liu¹, Yuchen Yuan¹, Wanjun Yu², Hang Yin¹, Zhao Yin¹, Yongting Zheng^{1,*}, Xiaodong He¹

¹ National Key Laboratory of Science and Technology on Advanced Composites in Special Environments, Center for Composite Materials and Structures, Harbin Institute of Technology, Harbin 150080, P. R. China

² School of Environment and Materials Engineering, Yantai University, Yantai 264003, P. R. China

* Corresponding author: zhengyt@hit.edu.cn

Abstract

Alumina toughened zirconia (ATZ) nanoceramics with high-strength, high-toughness and high-hardness were prepared by in-situ nanoprecipitation from solid solution micro-powders. The submicron Al₂O₃ (~450 nm) and ZrO₂ (~350 nm) grains contained low-density precipitated nano-ZrO₂ (~40 nm) and nano-Y₄Al₂O₉ (YAM, ~90 nm) particles, respectively, making high-performance nano-ATZ ceramics with ultrafine intracrystalline nanostructure yet achieved. There was a parallel or eutectic lattice orientation relationship between the submicrocrystals and its internal nanoparticles of their crystal planes, which is very conducive to the improvement of the mechanical properties of nano-ATZ ceramics. The fracture toughness and hardness of 30wt%Al₂O₃/70wt%ZrO₂(3mol%Y₂O₃) can be as high as 5.68 ± 0.17 MPa·m^{1/2} (single-edge V-notched beam method, SEVNB) and 16.32 ± 0.45 GPa, respectively, which are improved by ~25 % and ~20 % compared with those of 3Y-TZP ceramics. Therefore, this method can be used to prepare nano-ATZ ceramics contained ultrafine nanoparticles and uniform distribution of Al₂O₃ phases.

Keyword: Microstructural evolution; Nano-ATZ; Solid solutions; Nanoprecipitation

1. Introduction

ZrO₂ ceramics are widely used because of its excellent strength and toughness due to its t-m phase transformation and fine microstructure [1-3]. However, ZrO₂ is sensitive to hydrothermal aging [4-6], and its hardness [2, 7] is lower than that of zirconia toughened alumina (ZTA) [8-9] and Al₂O₃ ceramics [10], which limits its use as biomaterials or wear-resistant devices. There have been some works to improve the

mechanical properties of ZrO₂ ceramics through the ATZ method to make them more reliable and stable [6,11-19].

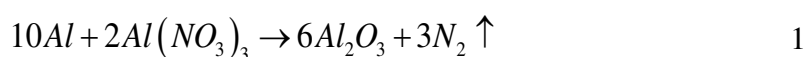
Zhang et al. [6] made 20wt%Al₂O₃/ZrO₂(2mol%Y₂O₃/0.4mol%La₂O₃) ceramics with toughness up to 7.1 MPa·m^{1/2} by conventional sintering and improved their aging stability. The hardness and toughness of the ATZ containing 20 wt% Al₂O₃ and 30 wt% Al₂O₃ prepared by Nevarez-Rascon et al. [12-13] were 16.05 GPa, 7.7 MPa·m^{1/2} and > 13 GPa, 6.9 MPa·m^{1/2}, respectively. The 20wt%Al₂O₃/ZrO₂(2.4mol% Y₂O₃) ceramics obtained by Govila et al. [18] through the hot isostatic pressing (HIP) had a flexural strength up to 1764 MPa. Li et al. [19] prepared 20wt%Al₂O₃/ZrO₂(3mol% Y₂O₃) ceramics with the flexural strength of 967 MPa and the toughness of 5.27 MPa·m^{1/2} by spark plasma sintering (SPS). Therefore, the hardness of ZrO₂ ceramics is greatly improved by these methods. However, fracture toughness of nano-ATZ ceramics is lower than that of 2Y-TZP (12.6 MPa·m^{1/2}) and 3Y-TZP (9.3 MPa·m^{1/2}) [2], indicating that nano-ATZ ceramics improve their hardness by sacrificing their toughness. Moreover, these nano-ATZ ceramics are mainly obtained by nanopowders, which have many problems such as easy agglomeration of powders, easy abnormal growth of grains during sintering and uneven distribution of Al₂O₃ phase. Hence, it is necessary to find a novel way to prepare nano-ATZ ceramics with high-strength, high-toughness and high-hardness.

In this paper, we prepared nano-ATZ ceramics containing 30 wt% Al₂O₃ by a new method of solid solution precipitation from micro-powders. This kind of powder with high-energy state and high supersaturation was obtained by combustion synthesis assisted spray atomization at 10~50 MPa and rapid water cooling [20-21]. In this method, the melt holding time is long (several minutes), so that the phases are fully fused to each other, and because of the ultra-high cooling rate, the powder has a very high degree of supersaturation [21], making it no longer dependent on the phase diagram [22]. The nano-ATZ ceramics sintered by this method had higher mechanical properties than those sintered by nanopowders, due to its ultrafine nanostructure and uniform distribution of Al₂O₃ phase by solid solution precipitation. Moreover, there are a few nanoparticles in Al₂O₃ and ZrO₂ grains, which exerts the effect of intracrystalline nano-toughening. This kind of microstructure is difficult to be realized by the previous preparation methods of nano-ATZ ceramics [6, 11-19]. More importantly, ZrO₂ contained unprecipitated Al₂O₃, which may be very beneficial to improve the aging resistance of ZrO₂ ceramics. Therefore, this method has far-reaching guiding significance for nano-ATZ ceramics.

2. Experimental Procedure

2.1 Raw materials and preparation of solid solution powders

The supersaturated 30 wt% Al₂O₃ + 70 wt% ZrO₂ (3 mol% Y₂O₃) solid solution powders (named as AZSSP, as shown in Fig. S1) with an average particle size of about 3 μm were obtained via combustion synthesis (Equation 1) assisted rapid water cooling (Fig. S2). The specific preparation method was detailed in our previous work [20-21]. This non-equilibrium solidification greatly improves the solid solubility of the two phases, making it no longer dependent on the phase diagram of Al₂O₃/ZrO₂ [22] (Fig. S3). The adiabatic temperature and the spray pressure of powder preparation were set to 4000 K and 20 MPa, respectively. The AZSSP was sieved through 200 mesh to obtain coarse and fine powders.



2.2 Preparation of nano-ATZ ceramics

The Al₂O₃/ZrO₂(3mol% Y₂O₃) nanoceramics were prepared via hot-press sintering (HP) using the fine powders with high energy ball milling for 1 hour and the vacuum hot-press furnace (ZYD-30-80, Jinzhou Aerospace Vacuum Equipment Co., Ltd., China) at the temperature of 1400 °C (ATZ-1400), 1450 °C (ATZ-1450) and 1500 °C (ATZ-1500) and the pressure of 40 MPa for 1 hour.

2.3 Characterization of AZSSP and ATZ

The microstructures were characterized with the Helios NanoLab 600i scanning electron microscope (SEM; FEI, USA) and back scattered electron imaging (BSE). The phase analysis was carried out by Empyrean Intelligent X-ray Diffraction Instrument (Panalytical Analytical Instruments Company, Netherlands). Microstructure characterization and super energy spectrum analysis were performed using the Talos F200X (FEI, U.S.) with ChemiSTEM technology (X-FEG and SuperX EDS) operated at 200 kV.

The four-point bending method was used to test the flexural strength of specimens (3 × 4 × 36 mm³), and the loading rate, span and bending arm length are 0.5 mm/min, 30 mm and 10 mm, respectively. The three-point bending method was used to test the fracture toughness of specimens (2 × 4 × 22 mm³), and the loading rate and span were 0.05 mm/min and 16 mm, respectively. There are two types of fracture toughness samples: single-edge notched beam (SENB) and single-edge V-notched beam (SEVNB). For SENB samples, a diamond saw with a thickness of 0.15 mm was used to cut the U-notch, and the ratio of notched depth to sample thickness was 0.35~0.6.

The SEVNB samples used a femtosecond laser (XIP-5/10/30) to quickly cut an ultra-sharp V-notch with the tip radius of about 0.6 μm on the root of the U-notch. In this paper, five specimens were tested for flexural strength and fracture toughness respectively, and the average value was taken as the final result. The calculation formulas of flexural strength and fracture toughness are shown in Equation 2 (GB/T 6569-2006 / ISO 14704:2000) and Equation 3 (GB/T 23806-2009 / ISO 15732:2003), respectively.

$$\sigma_f = \frac{3Fa}{wh^2} \quad 2$$

$$K_{Ic} = \frac{PL}{hw^{3/2}} \times Y\left(\frac{l}{w}\right) \quad 3$$

$$Y\left(\frac{l}{h}\right) = \frac{3}{2} \times \left(\frac{l}{h}\right)^{1/2} \times \frac{1.99 - \frac{l}{h} \left(1 - \frac{l}{h}\right) \left[2.15 - 3.93 \frac{l}{h} + 2.7 \left(\frac{l}{h}\right)^2\right]}{\left(1 + 2 \frac{l}{h}\right) \left(1 - \frac{l}{h}\right)^{3/2}} \quad 4$$

where, σ_f is the flexural strength, F and P are the bending load, a is the bending arm length, w is the width of the sample, h is the thickness of the sample, K_{Ic} is the fracture toughness, L is the span, l is the notched depth and $Y(l/h)$ is the form factor (as shown in Equation 4).

The Archimedes drainage method was used to test the relative density of ATZ. The Vickers hardness (Equation 5, GB/T 16534-1996) of the polished ATZ was measured by HVS-30 (Shanghai Shangcai Testing Machine Co., Ltd., China) with the loading force and loading time of 5 Kg and 15 s, respectively. Since $c/a > 1.25$ (where c is the distance between the indentation center and the crack tip and a is the half diagonal length of the indentation impression, Fig. S4), Equation 6 [23] was used to calculate the indentation fracture toughness (K_{Ic}) in indentation method (IM). The average values of relative density, Vickers hardness and fracture toughness calculated by indentation were obtained via 5 effective measurements.

$$H_v = 1.8544 \frac{F}{\left(\frac{d_1 + d_2}{2}\right)^2} \quad 5$$

$$K_{Ic} = 0.016 \left(\frac{E}{H_v}\right)^{1/2} P c^{3/2} \quad 6$$

where, Hv is the Vickers hardness, F and P are the bending load, d_1 and d_2 are the two diagonal lines of the indentation, E is the elastic modulus (approximately 247 GPa) and c is the distance between the indentation center and the crack tip.

The t-m phase transformation of ZrO_2 can be estimated by the t- $ZrO_2(101)$, m- $ZrO_2(\bar{1}11)$ and m- $ZrO_2(111)$ crystal planes of XRD phase peaks on the surface and fracture for ATZ samples (SENB and SEVNB), as shown in Equations 7, 8 [24].

$$V_m = \frac{1.311X_m}{1+0.311X_m} \quad 7$$

$$X_m = \frac{I_m(\bar{1}11)+I_m(111)}{I_m(\bar{1}11)+I_t(101)+I_m(111)} \quad 8$$

where, V_m and I represent the volume fraction and integrated intensity of the t-m ZrO_2 phases, respectively.

3. Results and Discussion

3.1 The analysis of AZSSP

Though the X-ray diffraction (XRD) analysis (Fig. 1a), most of the Al_2O_3 phase in the AZSSP was dissolved into ZrO_2 . Therefore, the lattice constant of 3Y- ZrO_2 became smaller because the radius of Al^{3+} is smaller than that of Zr^{4+} . The $a = b = 3.6008 \text{ \AA}$ and $c = 5.1793 \text{ \AA}$ (PDF #83-0113) of the fine powder became $a = b = 3.5989 \text{ \AA}$ and $c = 5.1475 \text{ \AA}$ (see Table 1 for details), respectively, and these values of the coarse powder became $a = b = 3.5987 \text{ \AA}$ and $c = 5.1519 \text{ \AA}$. The fine powder (6.05 wt%) contained more $Y_4Al_2O_9$ (YAM) phase than the coarse powder (1.80 wt%), and the former (18.86 wt%) had more m- ZrO_2 phase than the latter (4.54 wt%) in Table 2 (semi-quantitative calculation from XRD), because Y_2O_3 in the former mainly formed YAM instead of stabilizing the ZrO_2 phase. The cooling rate of coarse powder is lower than that of fine powder, so $\alpha-Al_2O_3$ phase appeared in the former, while only $\gamma-Al_2O_3$ existed in the latter (Fig. 1a). The fine powder contained a small amount of precipitated nanospheres, while the coarse powder contained more spheres and a lot of pores, as shown in Fig. 1. This is because large particles of Al_2O_3/ZrO_2 melt are ejected from the nozzle, leaving a small amount of gas remaining in the melt to form pores. In addition, the rapidly cooling water enters the melt and vaporizes into water vapor, which also forms holes. These nanospheres are composed of ZrO_2 -rich solid solution, from the BSE image of Fig. 1d, and they are surrounded by Al_2O_3 -rich solid solution.

3.2 The microstructure and mechanical properties of nano-ATZ

ATZ-1400, ATZ-1450 and ATZ-1500 were successfully obtained by AZSSP after HP. From the BSE images of their surfaces (Fig. 2), the Al₂O₃ phase was evenly distributed among the ZrO₂ grains. As the temperature increased, the grain size of Al₂O₃ gradually became larger. ATZ-1500 had abnormally grown Al₂O₃ grains with a size of 1-2 μm. The average grain sizes of ZrO₂ and Al₂O₃ are 350 nm and 450 nm, respectively, from the TEM and STEM images of ATZ-1450 (Fig. 3, Fig. 4 and Fig. S5). The Al₂O₃ crystal contains a small amount of nano-ZrO₂ particles with diameter of ~40 nm, and the ZrO₂ crystal also contains nano-YAM particles (see Fig. 7b for detailed analysis) with diameter of ~90 nm. This ultrafine structure will be very beneficial to improve the properties of nano-ATZ ceramics.

The STEM-EDX mapping and line scan analysis of ATZ-1450 in Fig. 5 and Fig. 6 show that a small amount of Al₂O₃ was not precipitated from ZrO₂. The unprecipitated Al₂O₃ acts as a stabilizer and inhibits the t-m phase transformation of ZrO₂, which may be very beneficial to the hydrothermal aging resistance of Y-TZP. The precipitated Al₂O₃ and the γ-Al₂O₃ in the AZSSP finally exist in the ceramic as the α-phase at high-temperature [21]. This was also confirmed by the selected area electron diffraction (SAED) of Al₂O₃ in area A, as shown in Fig. 5a, 5b. The ZrO₂ existed in the form of m- and t-phase from the SAED of ZrO₂ grains in area B and C (Fig. 5c, 5d). At the same time, t-ZrO₂ had a superlattice structure due to the presence of Y₂O₃ and incompletely precipitated Al₂O₃. The nanocrystals inside Al₂O₃ and ZrO₂ were further studied by high resolution transmission electron microscope (HRTEM) and fast Fourier transform (FFT) in Fig. 7. The nanocrystals in the ZrO₂ are YAM (Fig. 7a, area I), and there is an orientation relationship of (111)m-ZrO₂//(222)YAM. Similarly, the nanocrystals in the Al₂O₃ are ZrO₂ (Fig. 7b, area I). However, due to the presence of Y₂O₃ stabilizers in ZrO₂, the area around the nano-ZrO₂ particles is YAP (Fig. 7b, area II), and these two phases form the eutectic lattice orientation relationship. Therefore, there is a small amount of YAP around the ZrO₂ nanoparticles in Al₂O₃ crystals. These unique structures are very helpful to improve the performance of ceramics.

The nano-ATZ ceramics prepared via this novel method had excellent mechanical properties. Their flexural strength (σ) and hardness (H_v) can be as high as 896 ± 58 MPa and 16.32 ± 0.45 GPa, respectively, as shown in Table 3. The flexural strength is similar to that of 3Y-TZP and ATZ ceramics [2, 12] but the hardness is increased by about 20 %. In order to accurately measure the fracture toughness of nano-ATZ ceramics, IM, SENB and SEVNB are used respectively. The U-notched root radius of the SENB specimen is about 100 μm (Fig. 8a), and the fracture toughness is greatly

overestimated [25]. Many studies [25-27] have shown that using a femtosecond laser to cut an ultra-sharp V-notch at the root of the U-notch (the SEVNB method) can be used to characterize the toughness of ceramics. When the V-notched tip radius is less than 1.5 to 3 times of the grain size [27-29], the fracture toughness of the ceramic can be accurately measured. The V-notched tip radius of nano-ATZ ceramics is $\sim 0.6 \mu\text{m}$ (Fig. 8b, 8c), which is much smaller than three times of their grain size, so the SEVNB method can accurately measure their fracture toughness. In addition, many studies [30-31] have shown that when the U-notched root radius is less than the depth of the V-notch, and the equivalent notch angle is less than 60° (as shown in Fig. 9a), the SEVNB method can truly measure the fracture toughness accurately. The U-notched root radius (r), the V-notched depth (l) and the equivalent notch angle (θ) of SEVNB samples for nano-ATZ ceramics are about $104 \mu\text{m}$, $165 \mu\text{m}$ and 45° (as shown in Fig. 9b), respectively. The $r/l \approx 0.63 < 1$ and $45^\circ < 60^\circ$, so SEVNB samples meet test standards and can accurately measure their fracture toughness. The fracture toughness of the ATZ-1450 sample was as high as $5.68 \pm 0.17 \text{ MPa}\cdot\text{m}^{1/2}$ (SEVNB), which was much lower than the measured values of IM ($6.97 \pm 0.24 \text{ MPa}\cdot\text{m}^{1/2}$) and SENB ($13.31 \pm 0.45 \text{ MPa}\cdot\text{m}^{1/2}$), as shown in Table 4. The test results of the ATZ-1400 and ATZ-1500 were also the same as that of ATZ-1450. Compared with SEVNB, the fracture toughness of IM and SENB were overestimated by $\sim 26.99\%$ and $\sim 138.40\%$, respectively, as shown in Table 5. The difference between SENB and SEVNB methods can be seen from their typical stress-displacement curves (Fig. 10a). For the SEVNB specimen (Fig. 10b), the V-notched tip provides the source of cracks. When the external loading reaches F_0 , the crack tip expands steadily and the stress begins to release at the crack tip, so the stress-displacement curve shows a smooth nonlinear change. Because ZrO_2 ceramics contains t-m phase transition, it has strong resistance to crack extension, so crack propagation can be seen in the stress-displacement curve of SEVNB. The crack expands steadily up to the maximum load (F_{max}) and then grows instability, and eventually the specimen fractures at the load of F^* . For SENB specimens (Fig. 10c), the bottom of the smooth U-notch cannot provide the source of cracks. When the external load increases to a certain value, crack induction, crack propagation and fracture occur simultaneously. Because the load required to induce a microcrack is much greater than that for crack propagation and specimen fracture, the fracture toughness measured by the SENB method is overestimated. The SENB sample has no crack propagation, leading to direct fracture of the sample, so the stress-displacement curve has no deflection (Fig. 10c).

Therefore, the SEVNB method can accurately measure the ceramic toughness of resistance to crack propagation.

The fracture surface morphology of nano-ATZ ceramics, as shown in Fig. 11, can further show the reasons for the high strength and high toughness of ceramics prepared by this method. The fracture surfaces of the ATZ-1400, ATZ-1450 and ATZ-1500 specimens are uneven (Fig. 11a, 11b, 11c), and there are a lot of crack deflection and crack bifurcation (Fig. 11d, 11e, 11f), which greatly increases the crack growth path and improves the strength and toughness of ceramics. The high-magnification BSE and SEM images (Fig. 12) of the fracture surface for ATZ-1400, ATZ-1450 and ATZ-1500 show that nano-ATZ ceramics mainly occur intergranular fracture, and Al_2O_3 phases are evenly distributed in the ZrO_2 matrix. The ATZ-1400 fracture surface (Fig. 12a, 12b) contains a lot of microcrack toughening, especially the evenly distributed Al_2O_3 phase deflects the cracks (pointed by red arrows in Fig. 12b), which is very beneficial to improve the toughness of ceramics. In addition, some ZrO_2 phases undergo transgranular fracture (pointed by green arrows in Fig. 12b), which makes the t-m phase transition as high as 9.72 % (SENB, as shown in Fig. 13 and Table 4) and 6.04 % (SEVNB), so its fracture toughness is as high as $5.53 \pm 0.15 \text{ MPa}\cdot\text{m}^{1/2}$ (SEVNB), which is higher than that of 3Y-TZP ($4.4 \text{ MPa}\cdot\text{m}^{1/2}$, SEVNB) and increased by about 25 % [27]. The fracture morphology of ATZ-1450 is similar to that of ATZ-1400, and there are also microcrack propagation and crack deflection toughening (pointed by red arrows in Fig. 12d and Fig. 14). The difference is that there are some particles pulled out (pointed by blue arrows in Fig. 12d), which greatly increases the toughness of ceramics. The cross-sectional STEM image (Fig. 14) of microcrack growth in ATZ-1450 provides a more visual representation of the toughening mechanism. The uniformly distributed Al_2O_3 phase causes intergranular or transgranular fracture to promote crack deflection, as shown in red and green arrows, respectively. Similarly, some ZrO_2 phases undergo transgranular fracture (pointed by blue arrows in Fig. 14), which makes the t-m phase transition as high as 10.58 % (SENB, as shown in Fig. 13 and Table 4) and 4.47 % (SEVNB). At the same time, the YAM in the ZrO_2 crystal makes the crack deflection again, as shown in the dashed area in Fig. 14. Furthermore, YAM and ZrO_2 have a unique orientation relationship (Fig. 7a), so transgranular fracture of ZrO_2 consumes a lot of energy, thereby greatly improving the fracture toughness of ceramics. ATZ-1500 also mainly occurs intergranular fracture (Fig. 12e, 12f), and the grain size is significantly larger than that of ATZ-1400 and ATZ-1450. Like ATZ-1450, ATZ-1500 also has particle pull-out toughening, as shown in blue arrows in Fig. 12f. In addition,

the large-size grains of ATZ-1500 contain a lot of small particles on the grain boundary (Fig. 12f), which greatly increases its crack propagation path, thereby improving the toughness of ceramics. The t-m phase transition of ATZ-1500 is as high as 13.45 % (SENB) and 3.15 % (SEVNB), as shown in Fig. 13 and Table 4. Therefore, nano-ATZ ceramics prepared by solid solution nanoprecipitation have ultra-fine microstructure and high mechanical properties.

4. Conclusion

In summary, nano-ATZ nanoceramics were successfully prepared via the solid solution nanoprecipitation. The submicron-sized ZrO₂ and Al₂O₃ grains contain nano-sized YAM and ZrO₂ particles, respectively. The flexural strength, fracture toughness and hardness of nano-ATZ can be as high as 896 ± 58 MPa, 5.68 ± 0.17 MPa·m^{1/2} (SEVNB) and 16.32 ± 0.45 GPa, respectively, because of the ultrafine structure by in-situ nanoprecipitation. Therefore, this method has important guiding significance for nano-ATZ ceramics with high-performance.

Data availability

Raw data were generated at Harbin Institute of Technology, China. Derived data supporting the findings of this study are available from the corresponding author YZ on request.

CRedit authorship contribution statement

Yongdong Yu: Conceptualization, Methodology, Data curation, Writing - original draft. **Xudong Liu:** Formal analysis. **Yuchen Yuan:** Conceptualization. **Wanjuan Yu:** Methodology, Resources. **Hang Yin:** Conceptualization. **Zhao Yin:** Formal analysis. **Yongting Zheng:** Writing - review & editing, Funding acquisition, Validation. **Xiaodong He:** Supervision, Validation, Investigation.

Declaration of Competing Interest

The authors declare that they have no known competing financial interests or personal relationships that could have appeared to influence the work reported in this paper.

Acknowledgements

This work was supported by the National Natural Science Foundation of China (Grant No. 91016014 and 51872062). We thank Harbin Jehot Advanced Materials Co., Ltd. (China) for help with the powder preparation.

References

- [1] Hannink RH, Kelly PM, Muddle BC. Transformation toughening in zirconia-containing ceramics. *J Am Ceram Soc* 2000, **83**: 461-487.
- [2] Vasylykiv O, Sakka Y, Skorokhod VV. Low-temperature processing and mechanical properties of zirconia and zirconia–alumina nanoceramics. *J Am Ceram Soc* 2003, **86**: 299-304.
- [3] Travitzky N, Bonet A, Dermeik B, et al. Additive manufacturing of ceramic-based materials. *Adv Eng Mater* 2014, **16**: 729-754.
- [4] Zhang F, Vanmeensel K, Inokoshi M, et al. Critical influence of alumina content on the low temperature degradation of 2–3 mol% yttria-stabilized TZP for dental restorations. *J Eur Ceram Soc* 2015, **35**: 741-750.
- [5] Lughì V, Sergo V. Low temperature degradation-aging-of zirconia: A critical review of the relevant aspects in dentistry. *Dent Mater* 2010, **26**: 807-820.
- [6] Zhang F, Chevalier J, Olagnon C, et al. Slow crack growth and hydrothermal aging stability of an alumina-toughened zirconia composite made from La₂O₃-doped 2Y-TZP. *J Eur Ceram Soc* 2017, **37**: 1865-1871.
- [7] Gogotsi GA. Fracture toughness of ceramics and ceramic composites. *Ceram Int* 2003, **29**: 777-784.
- [8] Zhan GD, Kuntz J, Wan J, et al. A novel processing route to develop a dense nanocrystalline alumina matrix (< 100 nm) nanocomposite material. *J Am Ceram Soc* 2003, **86**: 200-2002.
- [9] Yu Y, Zheng Y, Yu W, et al. Evolution of interfacial microstructures between tungsten wires/flakes or graphite flakes and Al₂O₃/ZrO₂ eutectic ceramics via a novel combustion synthesis centrifugal casting. *Ceram Int* 2019, **45**: 14742-14748.
- [10] Riu DH, Kong YM, Kim HE. Effect of Cr₂O₃ addition on microstructural evolution and mechanical properties of Al₂O₃. *J Eur Ceram Soc* 2000, **20**: 1475-1481.
- [11] Schneider J, Begand S, Kriegel R, et al. Low-temperature aging behavior of alumina-toughened zirconia. *J Am Ceram Soc* 2008, **91**: 3613-3618.
- [12] Borunda EO, Elguezabal AA. Al₂O_{3(w)}–Al₂O_{3(n)}–ZrO₂(TZ-3Y)_n multi-scale nanocomposite: An alternative for different dental applications? *Acta Biomater* 2010, **6**: 563-570.
- [13] Nevarez-Rascon A, Aguilar-Elguezabal A, Orrantia E, et al. On the wide range of mechanical properties of ZTA and ATZ based dental ceramic composites by

- varying the Al₂O₃ and ZrO₂ content. *Int J Refract Met Hard Mater* 2009, **27**: 962-970.
- [14] Borlaf M, Szubra N, Serra-Capdevila A, *et al.* Fabrication of ZrO₂ and ATZ materials via UV-LCM-DLP additive manufacturing technology. *J Eur Ceram Soc* 2020, **40**: 1574-1581.
- [15] Verga F, Borlaf M, Conti L, *et al.* Laser-based powder bed fusion of alumina toughened zirconia. *Addit Manuf* 2020, **31**: 100959.
- [16] Ai Y, Xie X, He W, *et al.* Microstructure and properties of Al₂O₃(n)/ZrO₂ dental ceramics prepared by two-step microwave sintering. *Mater Des* 2015, **65**: 1021-1027.
- [17] Nevarez-Rascon A, Aguilar-Elguezabal A, Orrantia E, *et al.* Compressive strength, hardness and fracture toughness of Al₂O₃ whiskers reinforced ZTA and ATZ nanocomposites: Weibull analysis. *Int J Refract Met Hard Mater* 2011, **29**: 333-340.
- [18] Govila R. Strength characterization of yttria-partially stabilized zirconia/alumina composite. *J Mater Sci* 1993, **28**: 700-718.
- [19] Li S, Izui H, Okano M, *et al.* Microstructure and mechanical properties of ZrO₂ (Y₂O₃)–Al₂O₃ nanocomposites prepared by spark plasma sintering. *Particuology* 2012, **10**: 345-351.
- [20] Yu Y, Lin F, Zheng Y, *et al.* High-density nanoprecipitation mechanism and microstructure evolution of high-performance Al₂O₃/ZrO₂ nanocomposite ceramics. *J Eur Ceram Soc* 2021, **41**: 5269-5279.
- [21] Yu Y, Zheng Y, Liu X, *et al.* Microstructure evolution of YSZ/Al₂O₃ supersaturated solid solution, *Appl Surf Sci* 2021, **549**: 149260.
- [22] ALPER AM. Science of ceramics, ed. G. H. Stewart, Academic Press, London, 1967, **339**.
- [23] Anstis GR, Chantikul P, Lawn BR, *et al.* A critical evaluation of indentation techniques for measuring fracture toughness: I, direct crack measurements. *J Am Ceram Soc* 1981, **64**: 533-538.
- [24] Toraya H, Yoshimura M, Somiya S. Calibration curve for quantitative analysis of the monoclinic-tetragonal ZrO₂ system by x-ray diffraction. *J Am Ceram Soc* 1984, **67**: 119-121.
- [25] Zhao W, Cui J, Rao P. Effect of molten zone ablated by femtosecond lasers on fracture toughness of Si₃N₄ measured by SEVNB method. *J Eur Ceram Soc* 2018, **38**: 2243-2246.

- [26] Turon-Vinas M, Anglada M. Fracture toughness of zirconia from a shallow notch produced by ultra-short pulsed laser ablation. *J Eur Ceram Soc* 2014, **34**: 3865-3870.
- [27] Cui J, Gong Z, Rao P. Effect of molten zone ablated by femtosecond laser on fracture toughness of oxide ceramics. *J Eur Ceram Soc* 2017, **38**: 2440-2444.
- [28] Nishida T, Hanaki Y, Pezzotti G. Effect of notch-root radius on the fracture toughness of a fine-grained alumina. *J Am Ceram Soc* 1994, **77**: 606-608.
- [29] Yang S, Zhang C, Zhang X. Notch radius effect on fracture toughness of ceramics pertinent to grain size. *J Eur Ceram Soc* 2020, **40**: 4217-4223.
- [30] Wang X, Atkinson A. On the measurement of ceramic fracture toughness using single edge notched beams. *J Eur Ceram Soc* 2015, **35**: 3713-3720.
- [31] Wang A, Du B, Hu P, et al. Reliable evaluation of fracture toughness in ceramics via nanosecond laser notching method. *J Eur Ceram Soc* 2019, **39**: 883-889.

Figure captions:

Fig. 1 (a) XRD patterns of AZSSP. The BSE images of cross-sections of fine powders (b) and coarse powders (c). (d) An enlarged view of the box area in Fig. (c). The light phase represents the ZrO_2 phase, and the dark phase represents the Al_2O_3 phase.

Fig. 2 The cross-sectional BSE pictures of ATZ-1400, ATZ-1450 and ATZ-1500. The bright phase and the dark phase represent the ZrO_2 phase and the Al_2O_3 phase, respectively.

Fig. 3 Cross-sectional TEM (a) and STEM (b) images of ATZ-1450. The bright phase and the dark phase in Fig. (b) represent the ZrO_2 phase and the Al_2O_3 phase, respectively.

Fig. 4 The size distribution of nano- ZrO_2 grains in the Al_2O_3 grains (a), nano- $Y_4Al_2O_9$ grains in the ZrO_2 grains (b), submicro- ZrO_2 grains (c) and submicro- Al_2O_3 grains (d) in Fig. 3(b). The average grain size of these four grains is about 40 nm, 90 nm, 350 nm and 450 nm, respectively.

Fig. 5 (a) Cross-sectional STEM image of ATZ-1450. (b), (c) and (d) images show the selected area electron diffraction (SAED) of regions A, B, and C in Fig. (a). (e), (f), (g) and (h): The STEM-EDX elemental mappings show the distribution of Al, O, Zr and Y elements, respectively.

Fig. 6 (a) STEM image of ATZ-1450. (b) The STEM-EDX composition profile at the arrow position in Fig. (a) shows the distribution of Al, O, Zr and Y elements, respectively.

Fig. 7 HRTEM images of nanoparticles inside ZrO_2 crystal (a) and Al_2O_3 crystal (b). I, II and III are enlarged images of different regions in Fig. (a) and Fig. (b), respectively. Insets in I and II are the corresponding FFT patterns.

Fig. 8 (a) The SEM image of SENB sample showing that the root radius of U-notch is about 100 μm . (b) The SEM image of SEVNB sample showing that a femtosecond laser is used to cut an ultra-sharp V-notch based on the U-notch. (c) An enlarged view of the V-notch with the tip radius of $\sim 0.6 \mu m$ (much less than three times the grain size of ceramics [27-29]) indicating that this method can accurately measure the fracture toughness of ceramics.

Fig. 9 (a) Schematic of the ultra-sharp V-notch with an equivalent notch angle (θ). The θ should be less than 60° and the U-notched root radius (r) should be less than the V-notched depth (l). (b) The SEM image of ceramic bar with an ultra-sharp V-notch based on the U-notch. The U-notched root radius (r), the V-notched depth (l) and the equivalent notch angle (θ) of SEVNB samples are about 104 μm , 165 μm and 45° , respectively. $r/l \approx 0.63 < 1$ and $45^\circ < 60^\circ$, so SEVNB samples meet test standards.

Fig. 10 (a) Stress-displacement graphs of SENB and SEVNB specimens. (b) and (c) are enlarged images of the dotted area in Fig. (a).

Fig. 11 The SEM images of fracture surface in the ATZ-1400 (a), ATZ-1450 (b) and ATZ-1500 (c). (d), (e) and (f) are the enlarged images of the dashed area in Figs. (a), (b) and (c).

Fig. 12 (a) and (b): The BSE images of fracture surface in the ATZ-1400. (c) and (d): The SEM images of fracture surface in the ATZ-1450. (e) and (f): The SEM images of fracture surface in the ATZ-1500.

Fig. 13 The XRD analysis of $(101)_t$, $(\bar{1}11)_m$ and $(111)_m$ crystal planes on fracture and surface of SENB (a) and SEVNB (b) samples.

Fig. 14 (a) Cross-sectional STEM image of microcrack growth in ATZ-1450. The red and green arrows show green intergranular and transgranular fracture of Al_2O_3 grains, respectively. The blue arrows represent the transcrystalline fracture of ZrO_2 , and the circled areas indicate that the nanoparticles inside the ZrO_2 grains promote crack deflection.

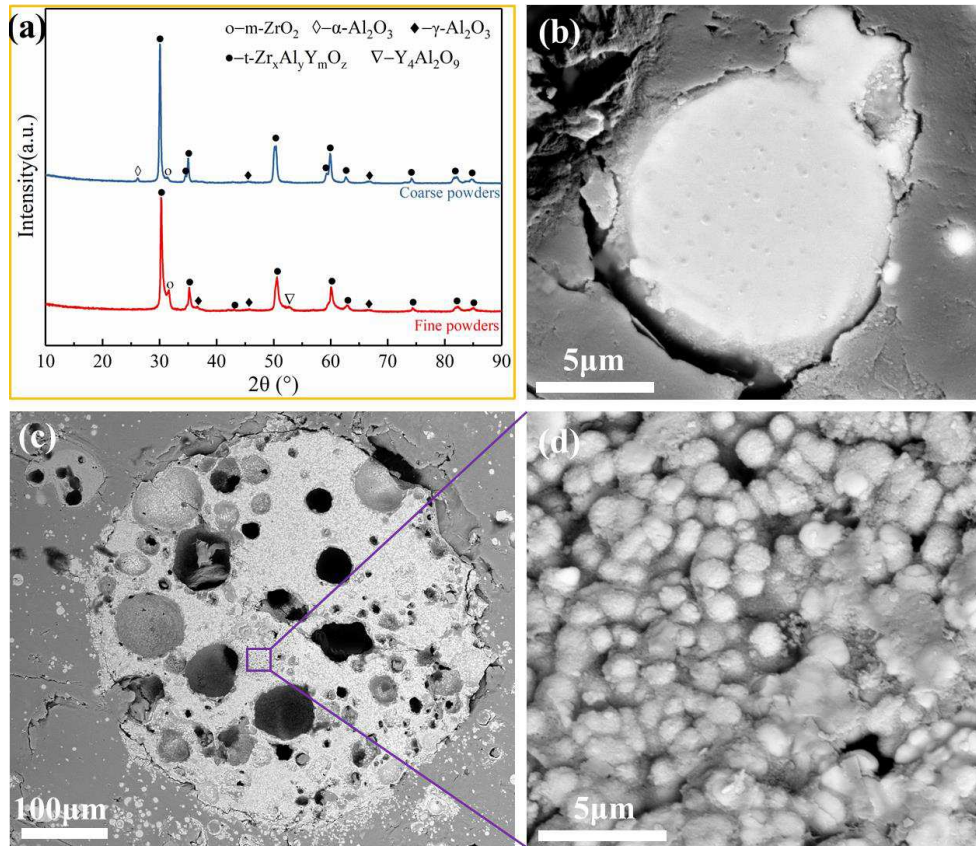


Fig. 1 (a) XRD patterns of AZSSP. The BSE images of cross-sections of fine powders (b) and coarse powders (c). (d) An enlarged view of the box area in Fig. (c). The light phase represents the ZrO₂ phase, and the dark phase represents the Al₂O₃ phase.

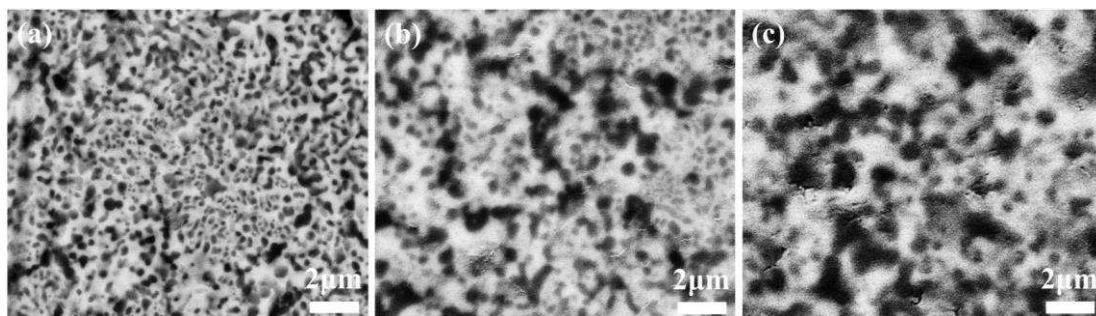


Fig. 2 The cross-sectional BSE pictures of ATZ-1400, ATZ-1450 and ATZ-1500. The bright phase and the dark phase represent the ZrO₂ phase and the Al₂O₃ phase, respectively.

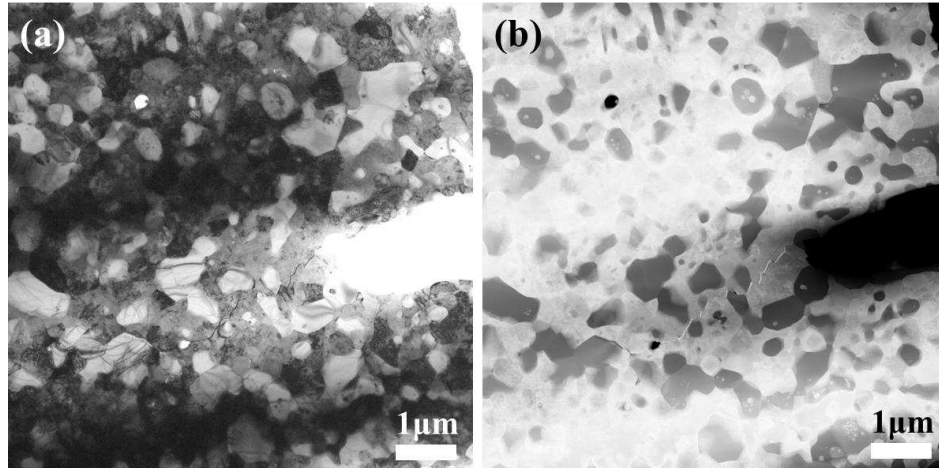


Fig. 3 Cross-sectional TEM (a) and STEM (b) images of ATZ-1450. The bright phase and the dark phase in Fig. (b) represent the ZrO_2 phase and the Al_2O_3 phase, respectively.

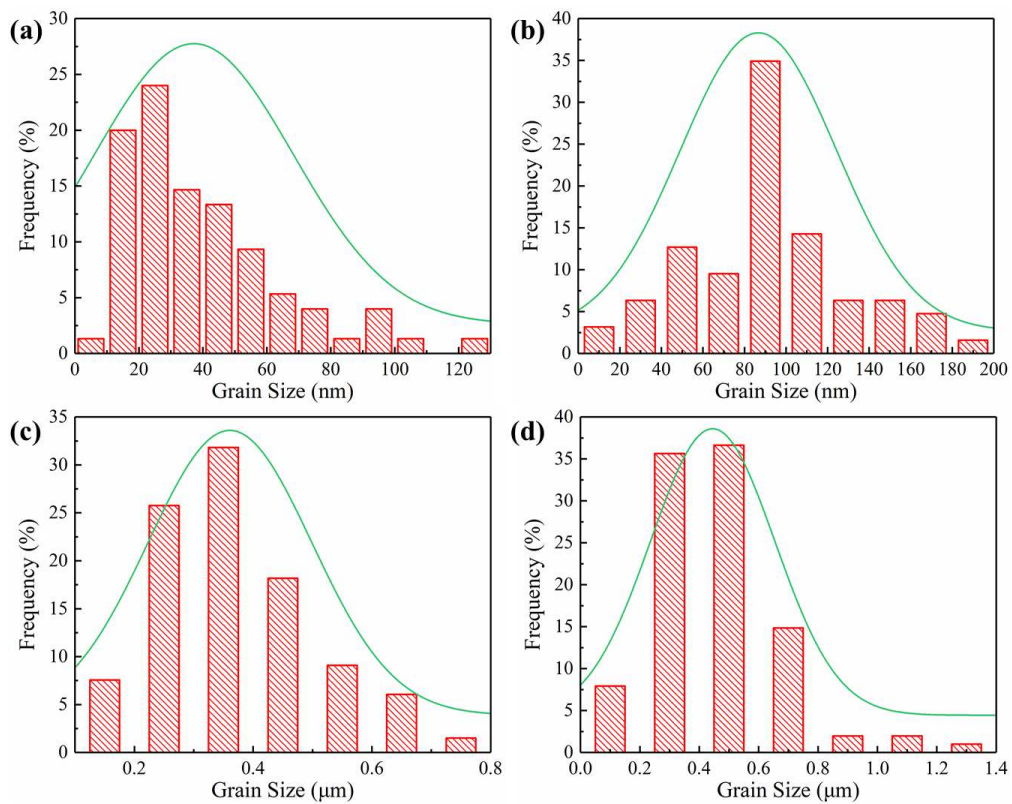


Fig. 4 The size distribution of nano- ZrO_2 grains in the Al_2O_3 grains (a), nano- $Y_4Al_2O_9$ grains in the ZrO_2 grains (b), submicro- ZrO_2 grains (c) and submicro- Al_2O_3 grains (d) in Fig. 3(b). The average grain size of these four grains is about 40 nm, 90 nm, 350 nm and 450 nm, respectively.

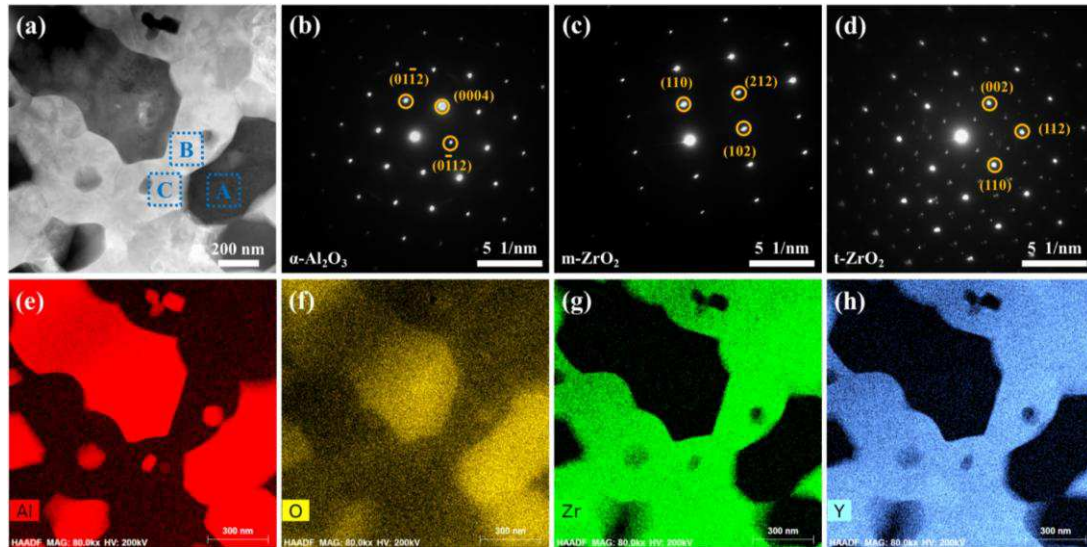


Fig. 5 (a) Cross-sectional STEM image of ATZ-1450. (b), (c) and (d) images show the selected area electron diffraction (SAED) of regions A, B, and C in Fig. (a). (e), (f), (g) and (h): The STEM-EDX elemental mappings show the distribution of Al, O, Zr and Y elements, respectively.

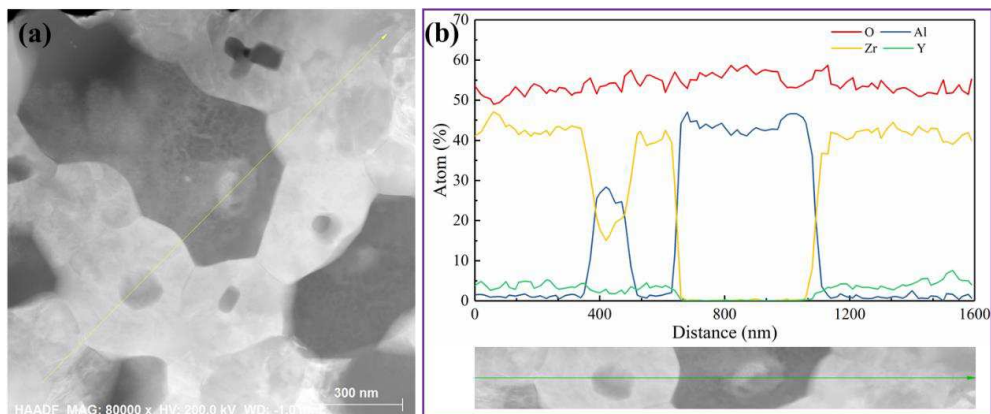


Fig. 6 (a) STEM image of ATZ-1450. (b) The STEM-EDX composition profile at the arrow position in Fig. (a) shows the distribution of Al, O, Zr and Y elements, respectively.

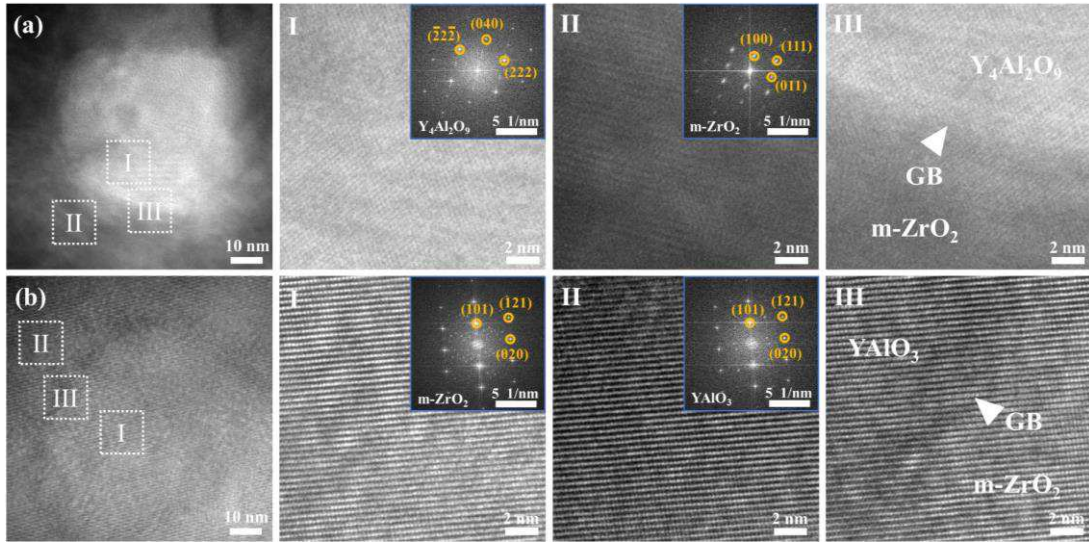


Fig. 7 HRTEM images of nanoparticles inside ZrO₂ crystal (a) and Al₂O₃ crystal (b). I, II and III are enlarged images of different regions in Fig. (a) and Fig. (b), respectively. Insets in I and II are the corresponding FFT patterns.

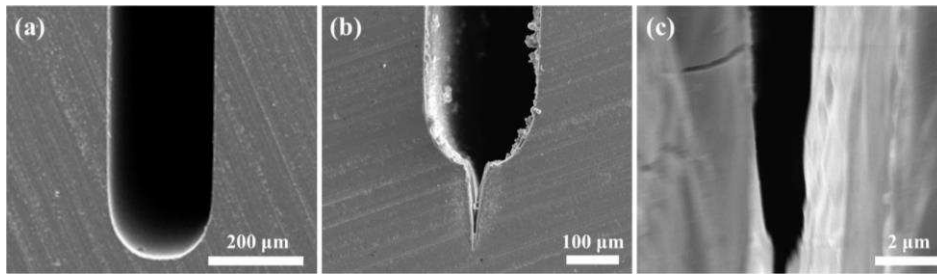


Fig. 8 (a) The SEM image of SENB sample showing that the root radius of U-notch is about 100 μm. (b) The SEM image of SEVNB sample showing that a femtosecond laser is used to cut an ultra-sharp V-notch based on the U-notch. (c) An enlarged view of the V-notch with the tip radius of ~0.6 μm (much less than three times the grain size of ceramics [27-29]) indicating that this method can accurately measure the fracture toughness of ceramics.

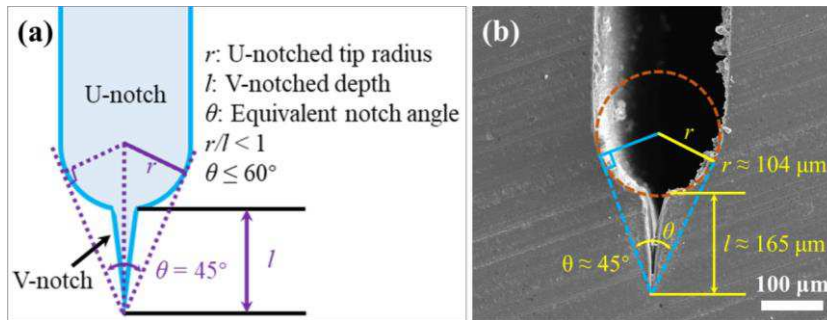


Fig. 9 (a) Schematic of the ultra-sharp V-notch with an equivalent notch angle (θ). The θ should be less than 60° and the U-notched root radius (r) should be less than the V-notched depth (l). (b) The SEM image of ceramic bar with an ultra-sharp V-notch based on the U-notch. The U-notched root radius (r), the V-notched depth (l) and the equivalent notch angle (θ) of SEVNB samples are about 104 μm, 165 μm and 45° , respectively. $r/l \approx 0.63 < 1$ and $45^\circ < 60^\circ$, so SEVNB samples meet test standards.

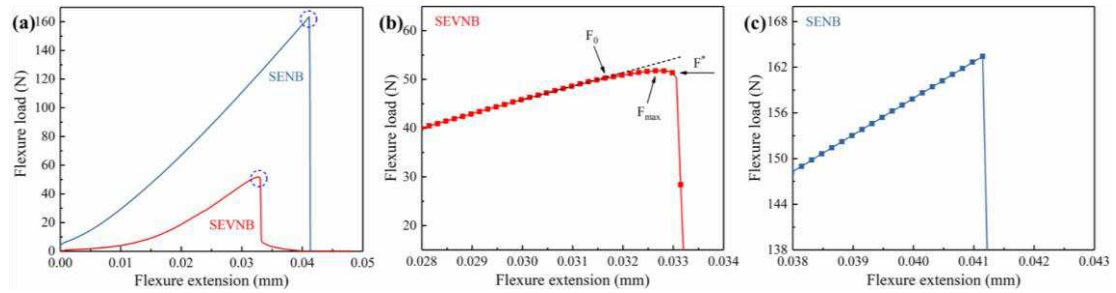


Fig. 10 (a) Stress-displacement graphs of SENB and SEVNB specimens. (b) and (c) are enlarged images of the dotted area in Fig. (a).

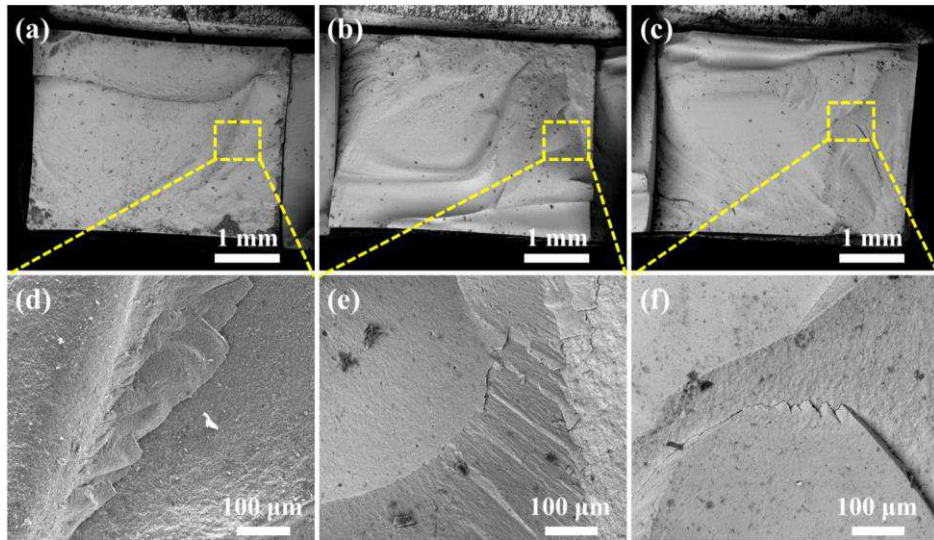


Fig. 11 The SEM images of fracture surface in the ATZ-1400 (a), ATZ-1450 (b) and ATZ-1500 (c). (d), (e) and (f) are the enlarged images of the dashed area in Figs. (a), (b) and (c).

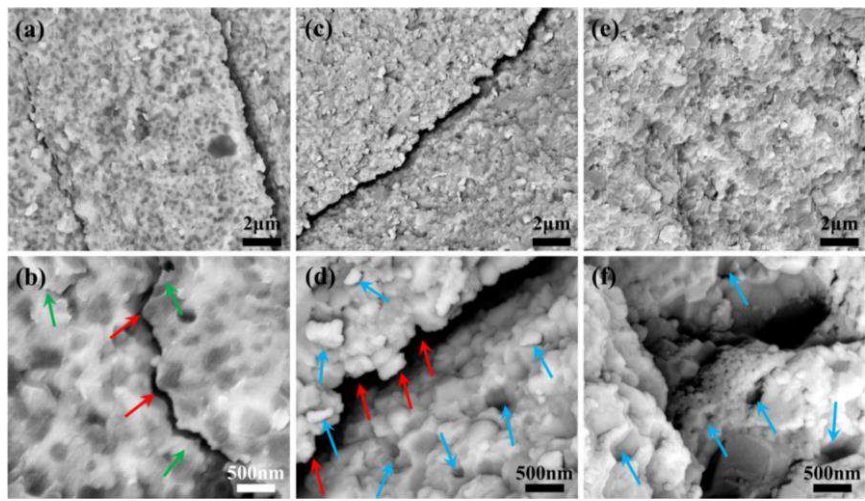


Fig. 12 (a) and (b): The BSE images of fracture surface in the ATZ-1400. (c) and (d): The SEM images of fracture surface in the ATZ-1450. (e) and (f): The SEM images of fracture surface in the ATZ-1500.

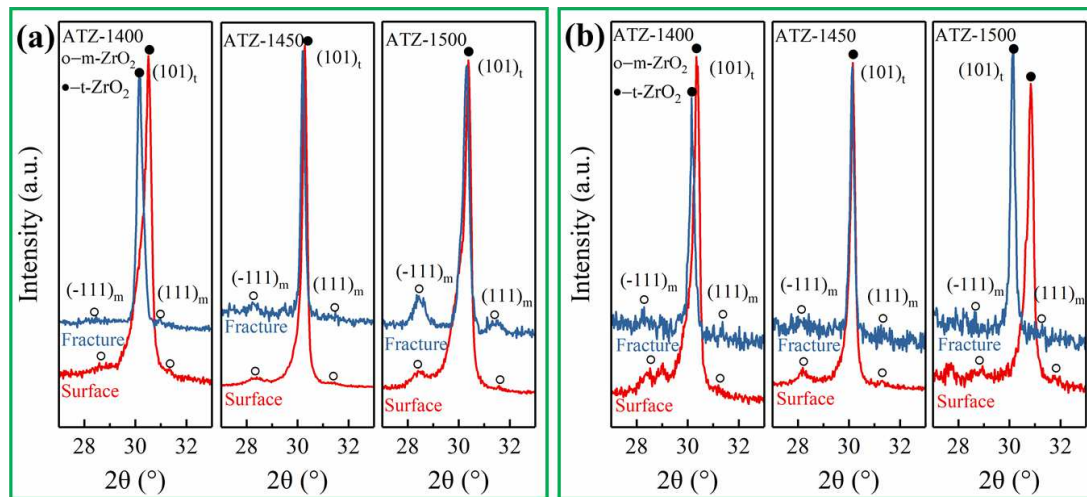


Fig. 13 The XRD analysis of $(101)_t$, $(\bar{1}11)_m$ and $(111)_m$ crystal planes on fracture and surface of SENB (a) and SEVNB (b) samples.

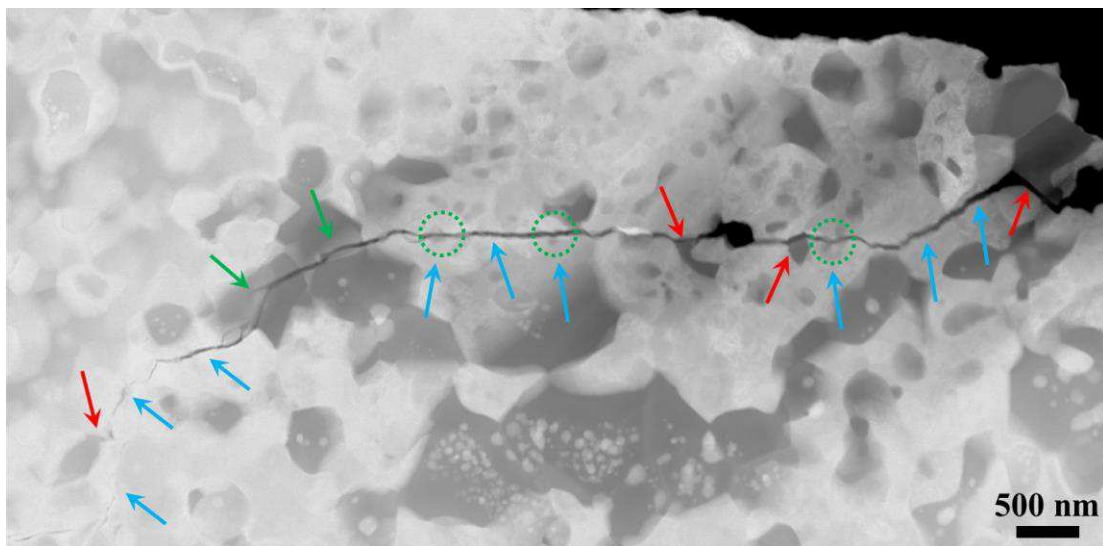


Fig. 14 (a) Cross-sectional STEM image of microcrack growth in ATZ-1450. The red and green arrows show green intergranular and transgranular fracture of Al_2O_3 grains, respectively. The blue arrows represent the transcrystalline fracture of ZrO_2 , and the circled areas indicate that the nanoparticles inside the ZrO_2 grains promote crack deflection.

Table captions:

Table 1 The lattice parameters and the unit cell volume of t-ZrO₂ measured by XRD.

Table 2 The phase content (Semi-quantitative calculation), crystallinity and average grain size obtained from the XRD pattern.

Table 3 Comparison of flexural strength (σ), Vickers hardness (H_v) and relative density of ATZ.

Table 4 Comparison of fracture toughness (K_{Ic}) of ATZ tested by IM, SENB and SEVNB methods.

Table 5 The percentage of K_{Ic} overestimated by IM and SENB methods in ATZ compared with SEVNB.

Table 1 The lattice parameters and the unit cell volume of t-ZrO₂ measured by XRD.

Component	Lattice parameters (Å)			Unit cell volume (Å ³)
	a	b	c	
PDF #83-0113 Zr _{0.963} Y _{0.037} O _{1.982}	3.6008	3.6008	5.1793	67.1536
Fine Powder	3.5989	3.5989	5.1475	66.6708
Coarse Powder	3.5987	3.5987	5.1519	66.7204

Table 2 The phase content (Semi-quantitative calculation), crystallinity and average grain size obtained from the XRD pattern.

Powder	Phase content (wt%)					Crystallinity (%)	Average grain size (nm)
	t-ZrO ₂	m-ZrO ₂	α-Al ₂ O ₃	γ-Al ₂ O ₃	Y ₄ Al ₂ O ₉ (YAM)		
Fine	50.25	18.86	0.00	24.84	6.05	87.55	33.0
Coarse	65.91	4.54	18.12	9.63	1.80	96.26	47.2

Table 3 Comparison of flexural strength (σ), Vickers hardness (H_v) and relative density of ATZ.

Sample	Flexural strength (σ , MPa)	Vickers hardness (H_v , GPa)	Relative density (%)
ATZ-1400	883 ± 76	16.32 ± 0.45	99.31
ATZ-1450	896 ± 58	15.78 ± 0.30	99.47
ATZ-1500	857 ± 81	15.09 ± 0.23	99.63

Table 4 Comparison of fracture toughness (K_{Ic}) of ATZ tested by IM, SENB and SEVNB methods.

Sample	Fracture toughness (K_{Ic} , MPa·m ^{1/2})			t-m phase transformation (vol%)	
	IM	SENB ($r \approx 100 \mu\text{m}$)	SEVNB ($r \approx 0.6 \mu\text{m}$)	SENB	SEVNB
ATZ-1400	7.18 ± 0.31	13.82 ± 0.55	5.53 ± 0.15	9.72	6.04
ATZ-1450	6.97 ± 0.24	13.31 ± 0.45	5.68 ± 0.17	10.58	4.47
ATZ-1500	7.05 ± 0.27	12.68 ± 0.52	5.49 ± 0.08	13.45	3.15

Table 5 The percentage of K_{Ic} overestimated by IM and SENB methods in ATZ compared with SEVNB.

Method	Overestimated percentage of K_{Ic} (%)			
	ATZ-1400	ATZ-1450	ATZ-1500	Average
IM	29.84	22.71	28.42	26.99
SENB	149.91	134.33	130.97	138.40

Figures

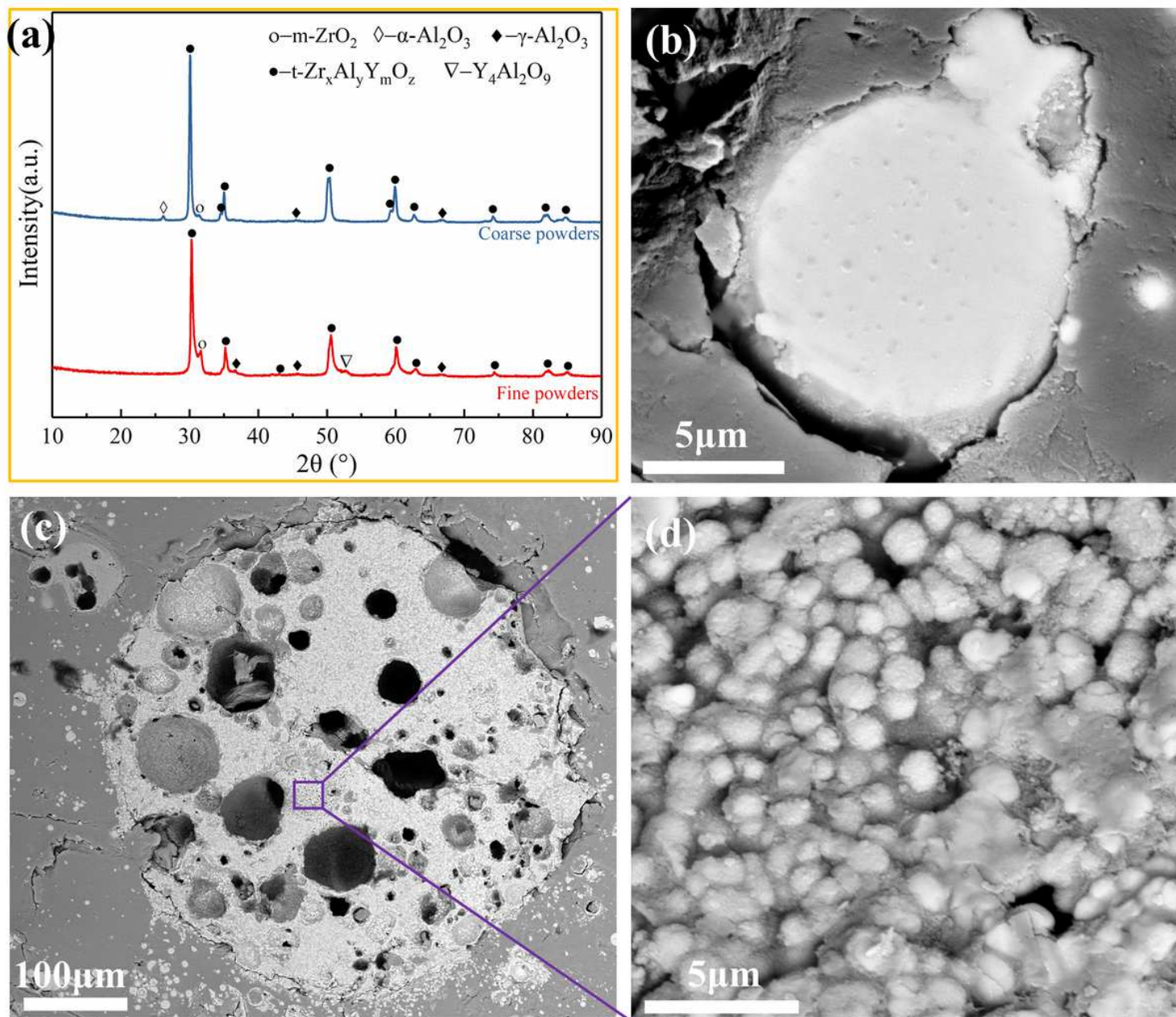


Figure 1

(a) XRD patterns of AZSSP. The BSE images of cross-sections of fine powders (b) and coarse powders (c). (d) An enlarged view of the box area in Fig. (c). The light phase represents the ZrO₂ phase, and the dark phase represents the Al₂O₃ phase.

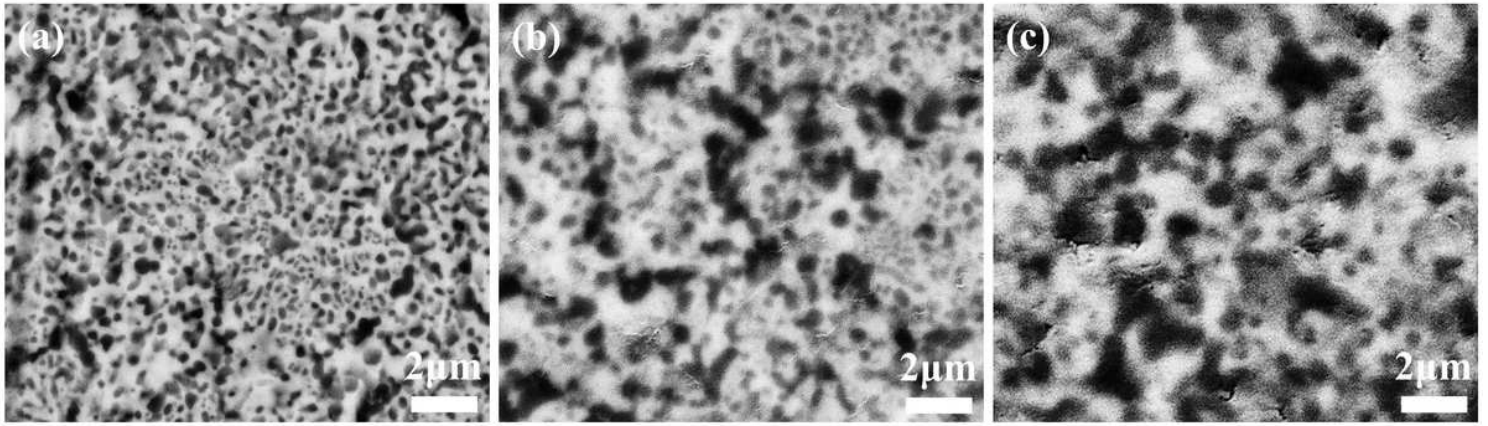


Figure 2

The cross-sectional BSE pictures of ATZ-1400, ATZ-1450 and ATZ-1500. The bright phase and the dark phase represent the ZrO_2 phase and the Al_2O_3 phase, respectively.

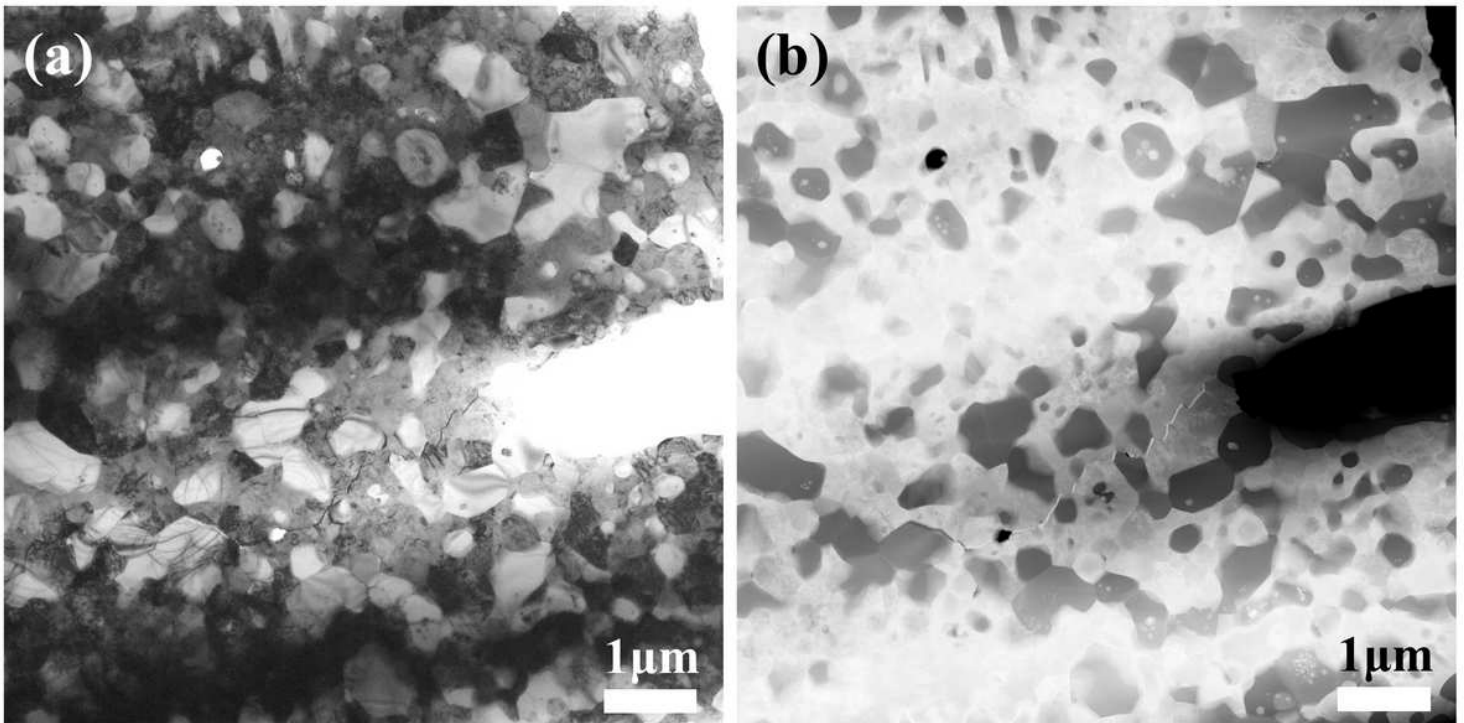


Figure 3

Cross-sectional TEM (a) and STEM (b) images of ATZ-1450. The bright phase and the dark phase in Fig. (b) represent the ZrO_2 phase and the Al_2O_3 phase, respectively.

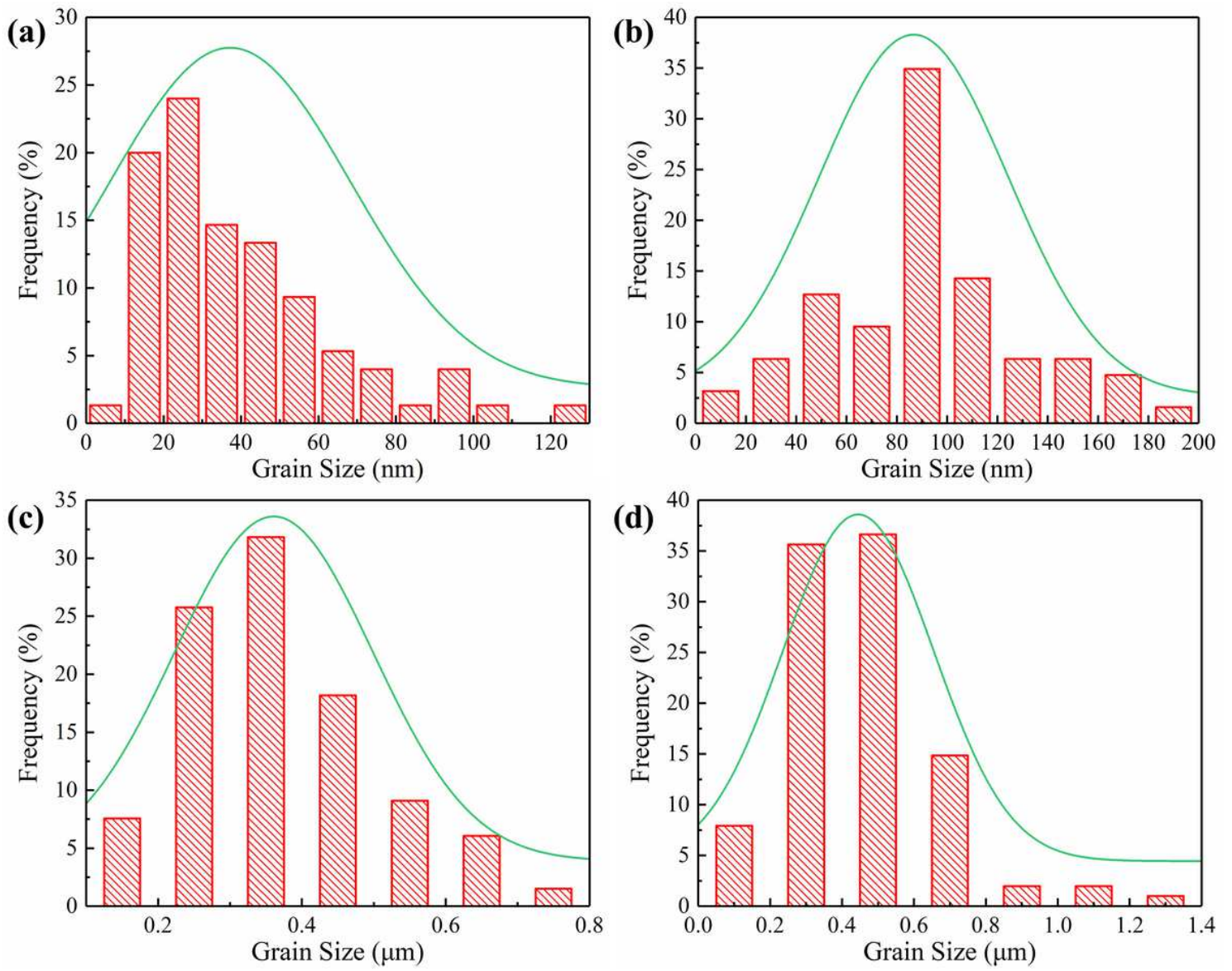


Figure 4

The size distribution of nano-ZrO₂ grains in the Al₂O₃ grains (a), nano-Y₄Al₂O₉ grains in the ZrO₂ grains (b), submicro-ZrO₂ grains (c) and submicro-Al₂O₃ grains (d) in Fig. 3(b). The average grain size of these four grains is about 40 nm, 90 nm, 350 nm and 450 nm, respectively.

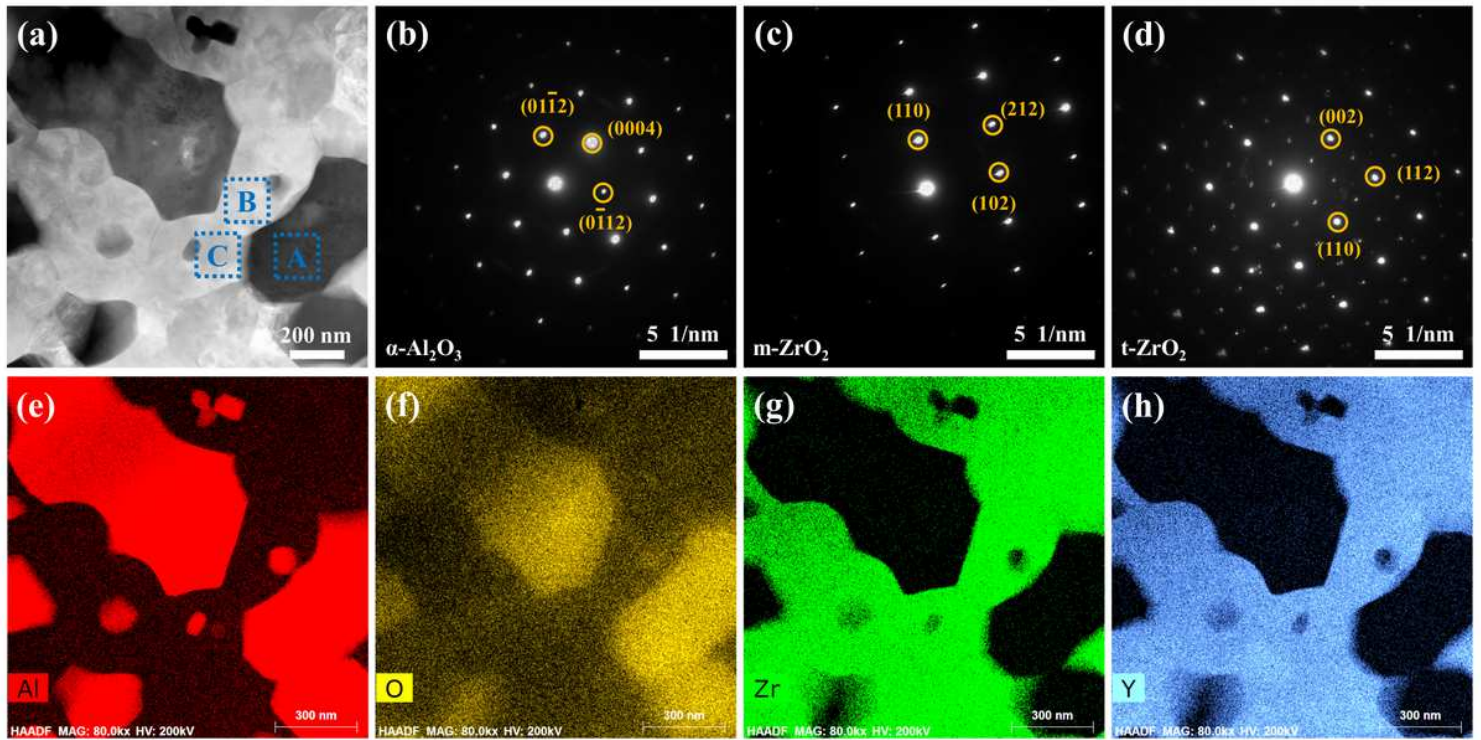


Figure 5

(a) Cross-sectional STEM image of ATZ-1450. (b), (c) and (d) images show the selected area electron diffraction (SAED) of regions A, B, and C in Fig. (a). (e), (f), (g) and (h): The STEM-EDX elemental mappings show the distribution of Al, O, Zr and Y elements, respectively.

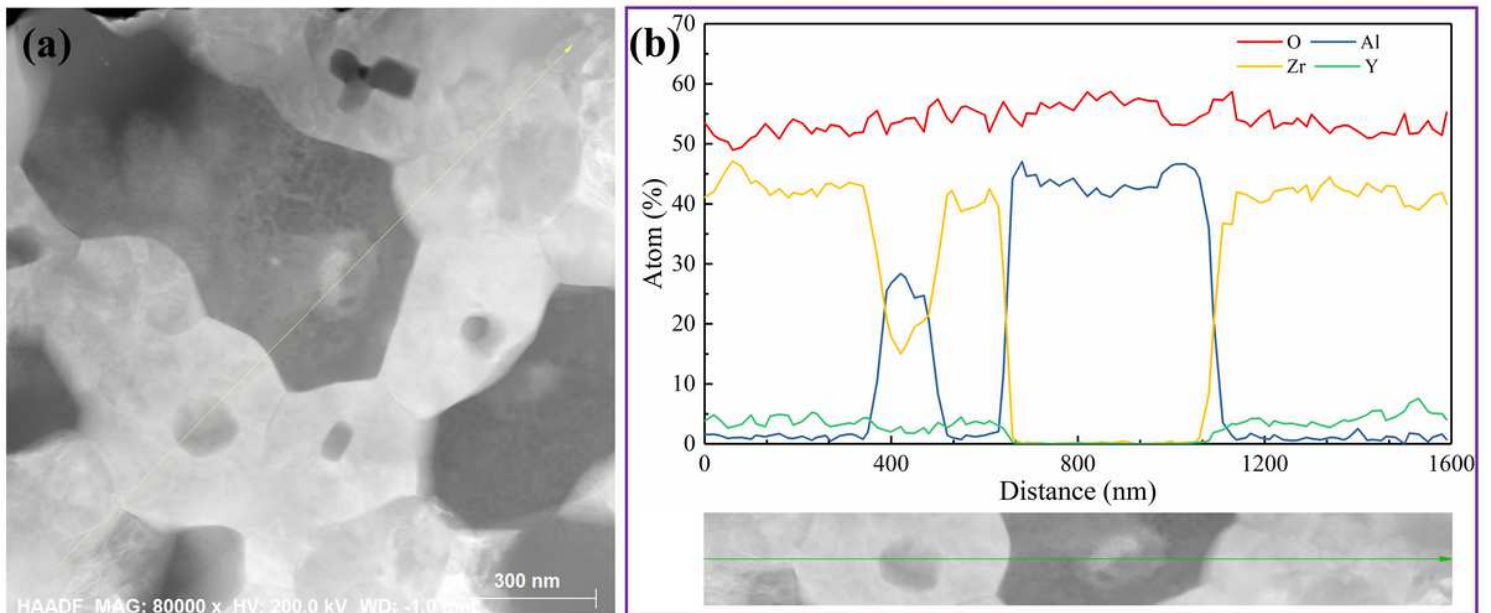


Figure 6

(a) STEM image of ATZ-1450. (b) The STEM-EDX composition profile at the arrow position in Fig. (a) shows the distribution of Al, O, Zr and Y elements, respectively.

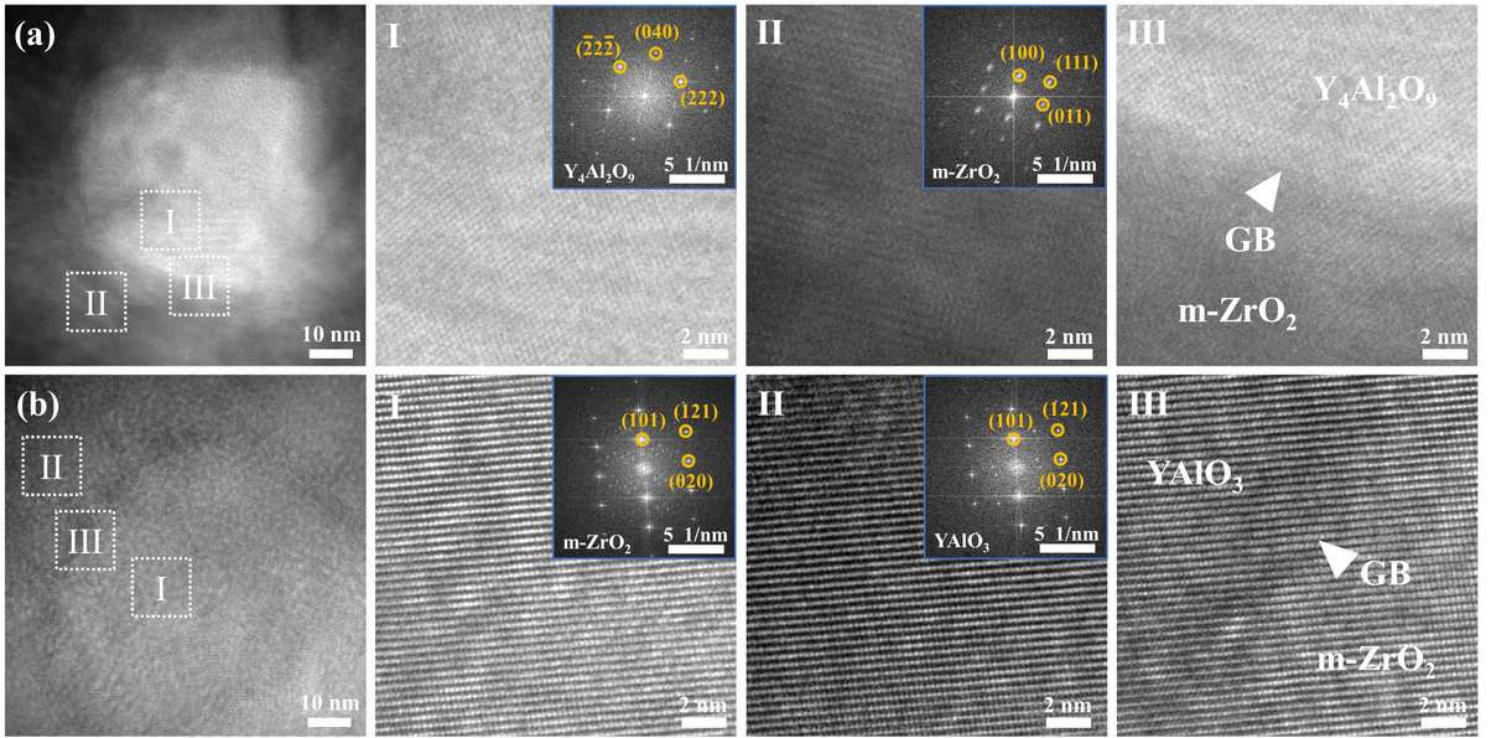


Figure 7

HRTEM images of nanoparticles inside ZrO₂ crystal (a) and Al₂O₃ crystal (b). I, II and III are enlarged images of different regions in Fig. (a) and Fig. (b), respectively. Insets in I and II are the corresponding FFT patterns.

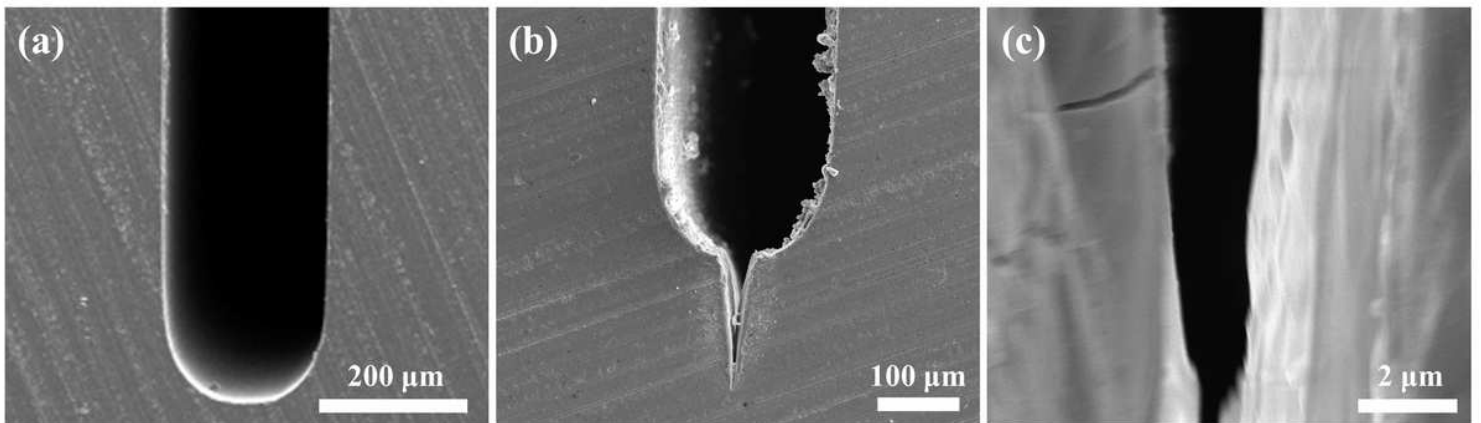


Figure 8

(a) The SEM image of SENB sample showing that the root radius of U-notch is about 100 μm. (b) The SEM image of SEVNB sample showing that a femtosecond laser is used to cut an ultra-sharp V-notch based on the U-notch. (c) An enlarged view of the V-notch with the tip radius of ~0.6 μm (much less than three times the grain size of ceramics [27-29]) indicating that this method can accurately measure the fracture toughness of ceramics.

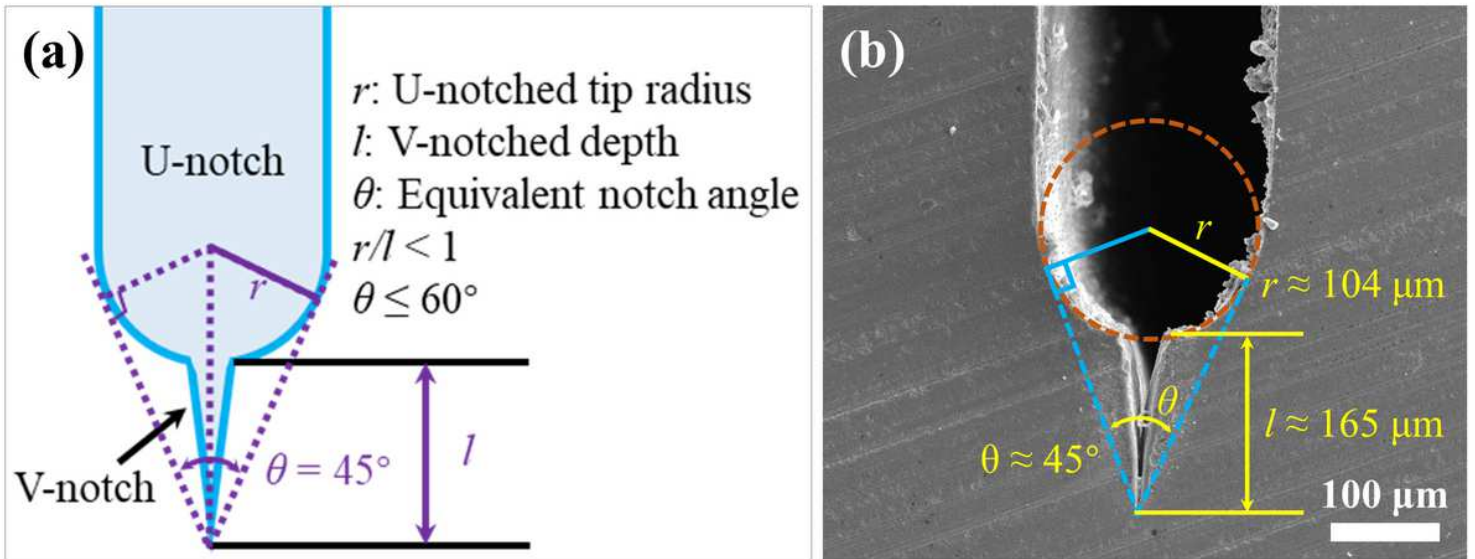


Figure 9

(a) Schematic of the ultra-sharp V-notch with an equivalent notch angle (θ). The θ should be less than 60° and the U-notched root radius (r) should be less than the V-notched depth (l). (b) The SEM image of ceramic bar with an ultra-sharp V-notch based on the U-notch. The U-notched root radius (r), the V-notched depth (l) and the equivalent notch angle (θ) of SEVNB samples are about $104 \mu\text{m}$, $165 \mu\text{m}$ and 45° , respectively. $r/l \approx 0.63 < 1$ and $45^\circ < 60^\circ$, so SEVNB samples meet test standards.

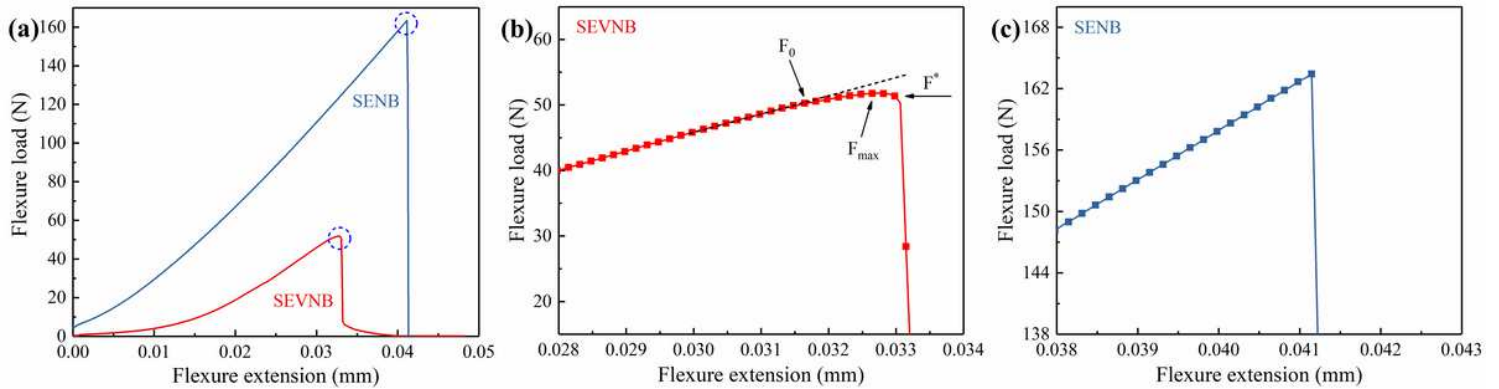


Figure 10

(a) Stress-displacement graphs of SENB and SEVNB specimens. (b) and (c) are enlarged images of the dotted area in Fig. (a).

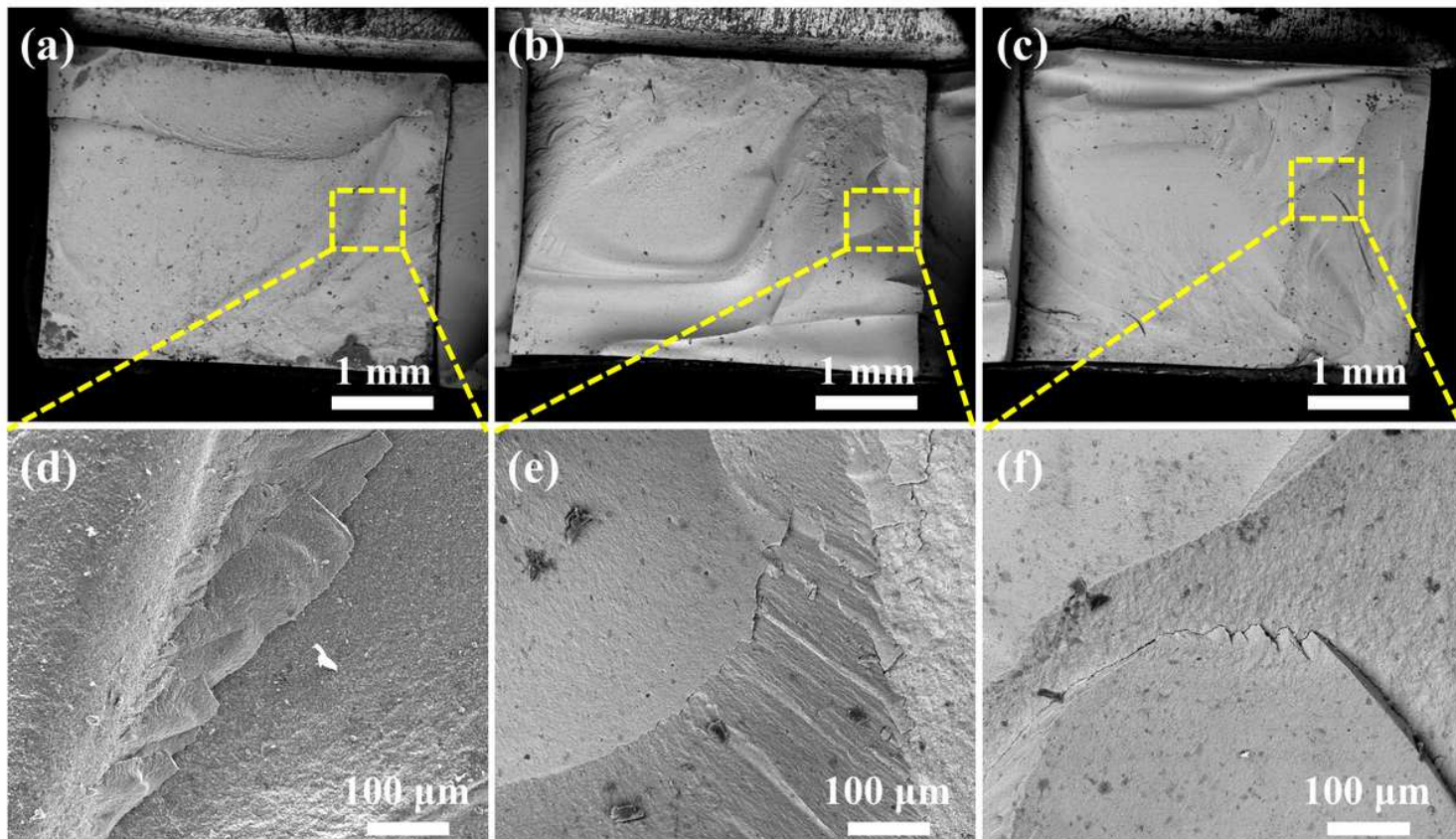


Figure 11

The SEM images of fracture surface in the ATZ-1400 (a), ATZ-1450 (b) and ATZ-1500 (c). (d), (e) and (f) are the enlarged images of the dashed area in Figs. (a), (b) and (c).

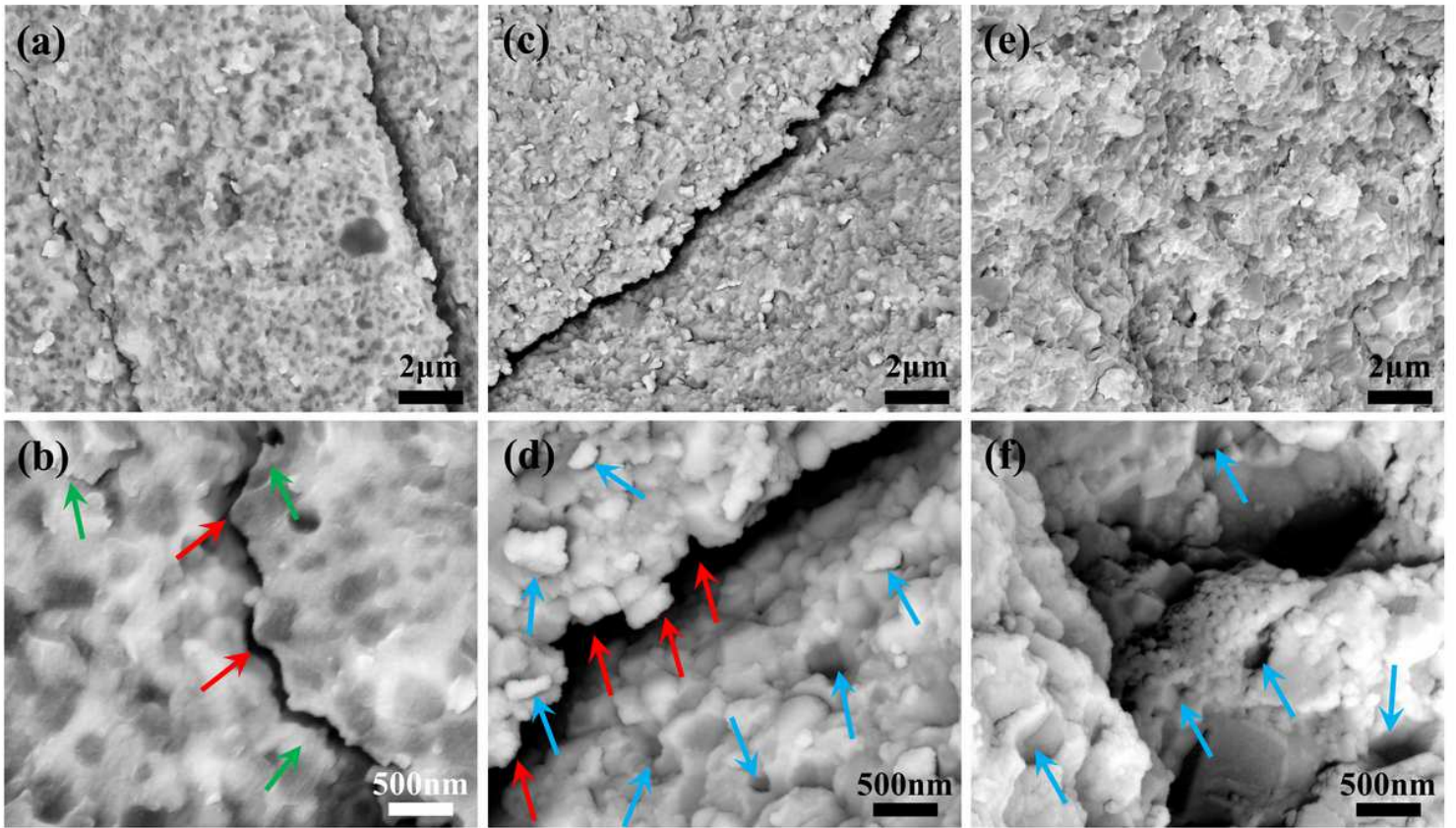


Figure 12

(a) and (b): The BSE images of fracture surface in the ATZ-1400. (c) and (d): The SEM images of fracture surface in the ATZ-1450. (e) and (f): The SEM images of fracture surface in the ATZ-1500.

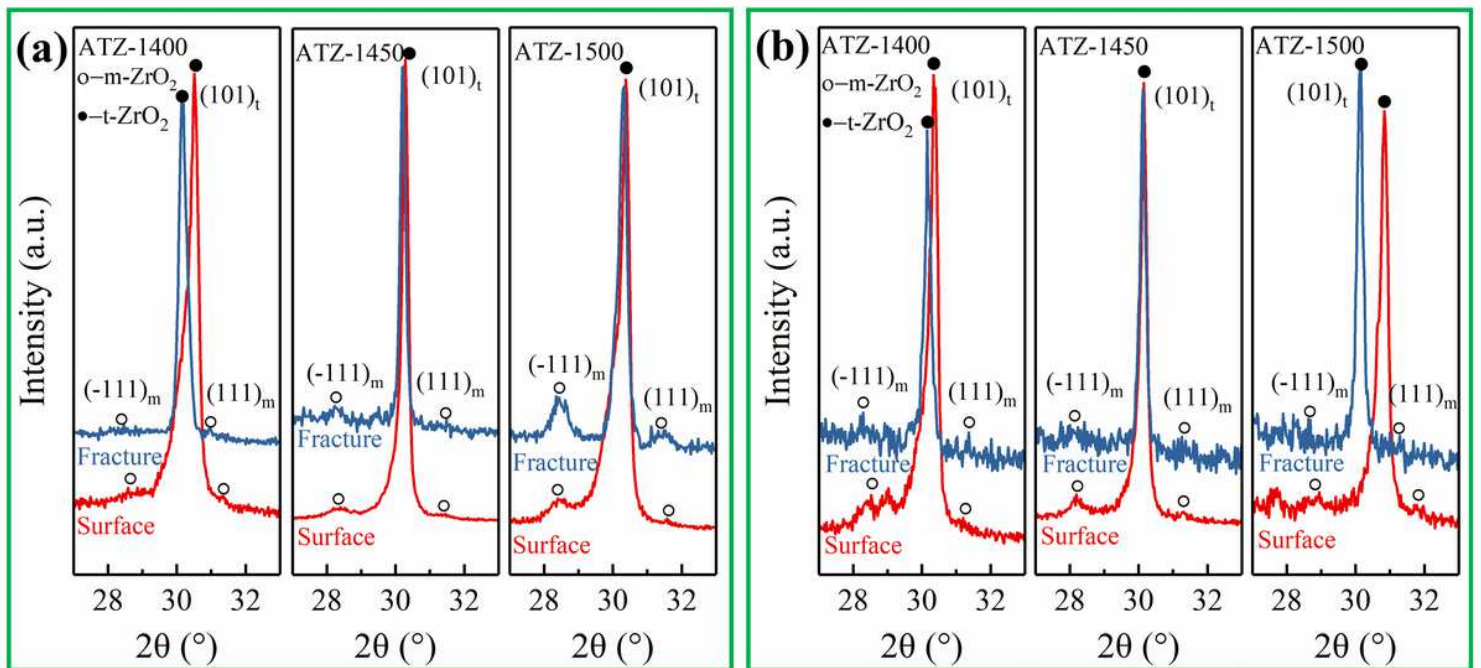


Figure 13

The XRD analysis of (101)t, ()m and (111)m crystal planes on fracture and surface of SENB (a) and SEVNB (b) samples.

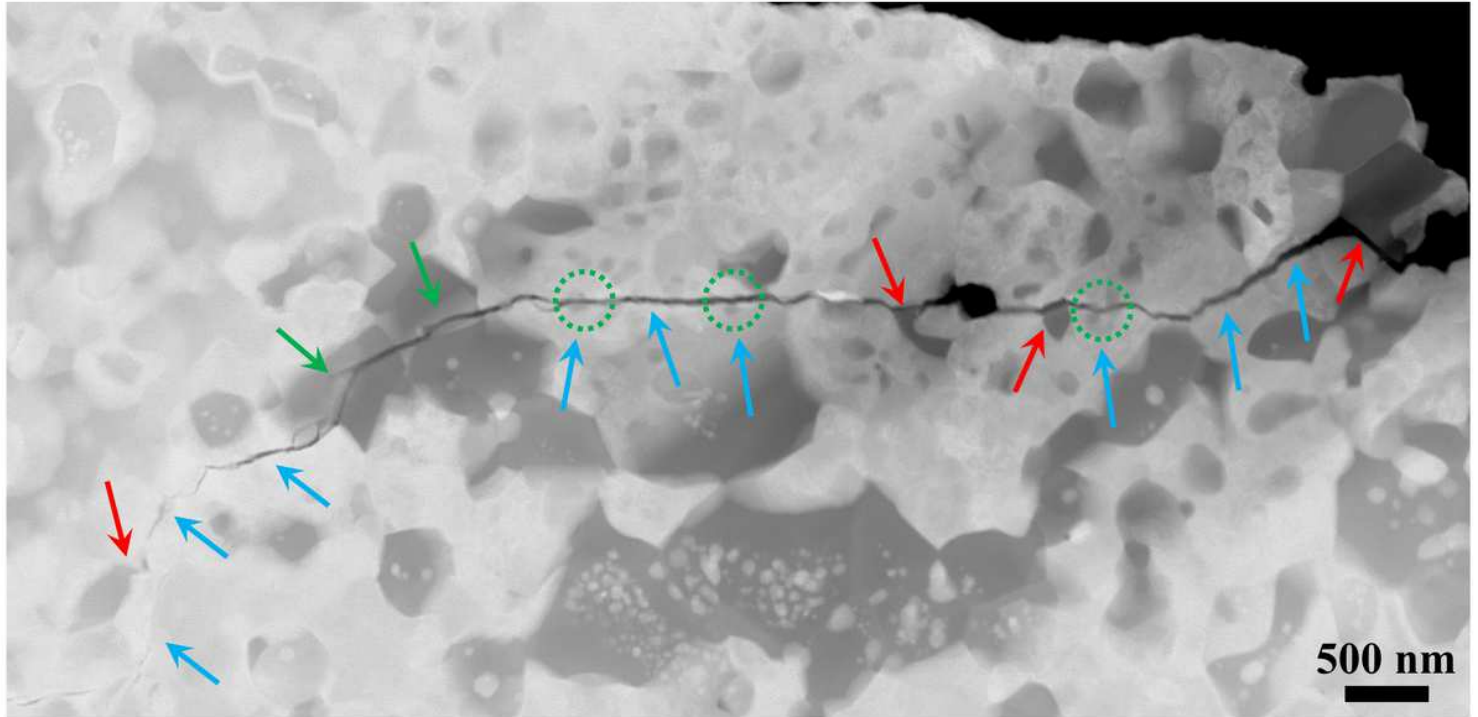


Figure 14

(a) Cross-sectional STEM image of microcrack growth in ATZ-1450. The red and green arrows show green intergranular and transgranular fracture of Al_2O_3 grains, respectively. The blue arrows represent the transcrystalline fracture of ZrO_2 , and the circled areas indicate that the nanoparticles inside the ZrO_2 grains promote crack deflection.

Supplementary Files

This is a list of supplementary files associated with this preprint. Click to download.

- [SupplementaryInformation.docx](#)